Nuclear pores as versatile reference standards for quantitative superresolution microscopy

Jervis Vermal Thevathasan[1,2,10], Maurice Kahnwald[1,10], Konstanty Cieśliński[1], Philipp Hoess [1,2], Sudheer Kumar Peneti[1,4], Manuel Reitberger[1,5], Daniel Heid [1,6], Krishna Chaitanya Kasuba[1,7], Sarah Janice Hoerner [1,8], Yiming Li [1], Yu-Le Wu[1,2], Markus Mund[1,9], Ulf Matti [1], Pedro Matos Pereira[3], Ricardo Henriques [3], Bianca Nijmeijer[1], Moritz Kueblbeck[1], Vilma Jimenez Sabinina [1], Jan Ellenberg [1] and Jonas Ries [1]*

Quantitative fluorescence and superresolution microscopy are often limited by insufficient data quality or artifacts. In this context, it is essential to have biologically relevant control samples to benchmark and optimize the quality of microscopes, labels and imaging conditions. Here, we exploit the stereotypic arrangement of proteins in the nuclear pore complex as in situ reference structures to characterize the performance of a variety of microscopy modalities. We created four genome edited cell lines in which we endogenously labeled the nucleoporin Nup96 with mEGFP, SNAP-tag, HaloTag or the photoconvertible fluorescent protein mMaple. We demonstrate their use (1) as three-dimensional resolution standards for calibration and quality control, (2) to quantify absolute labeling efficiencies and (3) as precise reference standards for molecular counting. These cell lines will enable the broader community to assess the quality of their microscopes and labels, and to perform quantitative, absolute measurements.

Superresolution microscopy, specifically single-molecule localization microscopy (SMLM, also known as PALM[1] or STORM[2]), reaches nanometer-scale optical resolution and provides structural insights into cell biological questions[3–5]. In SMLM, many factors have to be optimized: microscope optics; settings and stability; imaging conditions; fluorophores and labeling technologies; sample preparation and analysis software. However, the field lacks a set of common practices for general optimization of these factors, which is essential for ensuring comparable quality between different laboratories and experimental reproducibility. Current algorithms for image quality control are limited as they require previous knowledge about the imaged structure[6,7]. Suboptimal performance in SMLM is therefore not readily detected, which severely limits biological discovery.

To address this challenge, researchers have turned to imaging suitable reference standards. Simulated images served as reference standards to benchmark various superresolution software[8]. Artificial reference structures such as DNA origami[9,10] allow positioning fluorophores at precise three-dimensional (3D) positions, but are limited in the choice of labels and are intrinsically different from intracellular biological structures. Cellular reference structures have included histones[1], mitochondria[11] and microtubules[12]. For instance, image resolution is often approximated by evaluating cross-sectional profiles of microtubules, which requires fixation methods incompatible with other cellular structures (particularly membrane proteins) and is prone to cherry-picking. Furthermore,

because these structures have highly abundant epitopes, acceptable images are obtained even for labeling efficiencies below 1%. Therefore, these references are not ideal to optimize labeling efficiencies, a major factor determining image quality in SMLM.

An ideal superresolution reference structure has a stereotypical structure in which its fluorescent labels are arranged at distances resolvable by the technique of choice and in defined numbers to allow quantifying labeling efficiencies; it uses common dyes and labeling approaches to resemble intracellular measurements and it is present in many copies in the cell for statistical accuracy.

The nuclear pore complex (NPC) fulfills all these requirements and thus represents a quantitative reference structure. It comprises ~30 different proteins and selectively transfers macromolecules across the nuclear membrane. For the human NPC, a high-resolution structural map of most nucleoporins was obtained by electron microscopy[13]. The NPC has been used to validate quantitative microscopy[14–17] and SMLM has provided insights into its structure[5,18], highlighting its versatility.

Here, we generated cell lines where the nucleoporin Nup96 is endogenously tagged with commonly used labels. We demonstrate that imaging these cell lines yields excellent reference data for all experimental parameters in quantitative superresolution microscopy. We show their use to (1) quantify microscope performance, resolution and calibration, (2) measure absolute labeling efficiencies, (3) optimize imaging conditions and (4) count protein numbers within a complex.
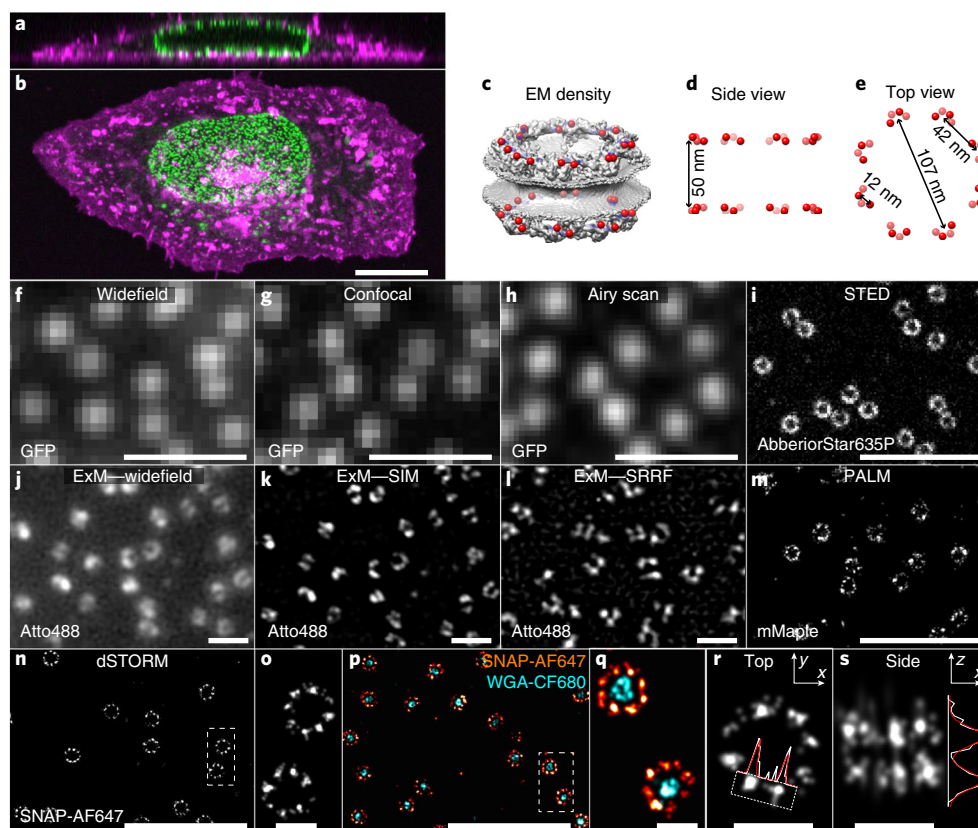
Fig. 1 | Nup96 cell lines. a,b, Representative confocal *xz* (**a**) and *xy* (**b**) image of the Nup96-GFP cell line. Green, Nup96-GFP; magenta, membranes (DiD). **c**, EM density of the NPC[13] with C termini of Nup96 indicated in red. **d,e**, Side view and top view schematic. **f–h**, Widefield (**f**), confocal (**g**) and Airy-scan images (**h**) of Nup96-GFP. **i**, Raw STED image of Nup96-GFP labeled with an AberriorStar635P-coupled anti-GFP nanobody. Resolution estimates based on Fourier power spectra for **f–i** can be found in Supplementary Fig. 3a. **j**, Widefield expansion microscopy image of Nup96-GFP labeled with an Atto488-coupled anti-GFP nanobody. **k**, Widefield expansion microscopy image of Nup96-GFP labeled as in **j**, but imaged using structured illumination. Estimates of the expansion factor based on the analysis of the ring diameters can be found in Supplementary Fig. 3c. **l**, Widefield expansion microscopy image of Nup96-GFP labeled as in **j**, but imaged using SRRF. **m–o**, SMLM image of Nup96-mMaple (**m**), SMLM of Nup96-SNAP labeled with BG-AF647 in GLOX/MEA (**n,o**). **p,q**, Dual-color SMLM image of Nup96-SNAP labeled with BG-AF647 (red) and WGA-CF680 (cyan) in GLOX/MEA. **r,s**, Corners of the NPC can be used as a resolution target in *x,y* (**r**) and *z* (**s**). Resolution estimates based on Fourier Ring Correlation for **m–q** can be found in Supplementary Fig. 3b. Representative images of one (**j–l**), two (**a,b,i**), three (**p–s**), four (**f–h,n,o**) or six (**m**) independent experiments are shown. Scale bars, 10 μm (**b**), 1 μm (**f–n,p**) and 100 nm (**o,q,r,s**).

Results

Generation of Nup96 cell lines. We identified Nup96 as a suitable reference protein (Fig. 1a–e). It is present in 32 copies per NPC where it forms a cytoplasmic and a nucleoplasmic ring, each consisting of 16 Nup96 copies. Each ring has eight corners that contain two Nup96, 12 nm apart[13]. The two rings are almost in register, thus the eight-fold symmetry of the NPC is clearly visible (Fig. 1e).

We generated homozygous knock-in U2OS cell lines (Supplementary Fig. 1, distributed by the CLS Cell Line Service), where Nup96 is endogenously labeled with one of four commonly used labels: mEGFP (subsequently referred to as green fluorescent protein (GFP)), the photoconvertible fluorescent protein mMaple[19], and the enzymatic labels SNAP-tag[20] and HaloTag[21]. In U2OS cells, the lower nuclear envelope is flat and close to the coverslip (Fig. 1a), thus hundreds of nuclear pores are in focus in a single widefield, confocal or total internal reflection (TIRF) (Supplementary Fig. 2) image.

Resolution and quality control. The Nup96 corners are from 10 to 100 nm apart, and are therefore suitable resolution standards for many microscopes. We first imaged our cells with nine microscopy approaches (Fig. 1f–n) and obtained images with excellent signal to noise ratio for all imaging modalities. Throughout all experiments,

we focused on the flat underside of the nucleus to avoid imaging tilted NPCs. For diffraction-limited techniques, NPCs act as sub-diffraction structures of defined brightness. Individual NPCs are resolved in widefield microscopy (Fig. 1f) and, with improved contrast in confocal microscopy (Fig. 1g). Airy-scan microscopy (Fig. 1h) leads to a visible but moderate improvement in resolution (Supplementary Fig. 3a). Stimulated emission depletion (STED[22]) microscopy resolves the ring-like arrangement (Fig. 1i).

These rings are also apparent in expansion microscopy (ExM[23]) with widefield (Fig. 1j), structured illumination (Fig. 1k) and SRRF (super-resolution radial fluctuations[24]) (Fig. 1l) readout. However, they appear less complete than in STED, PALM or STORM, indicating loss of labeling during expansion. Our reference cell lines can be used to directly infer the local expansion factor from the size of the rings[25] (Supplementary Fig. 3c and Methods). The measured local expansion factor of 3.2 was different from the global expansion factor of 4.5, indicating inhomogeneous expansion[26], which potentially complicates ExM of protein complexes.

SMLM using mMaple (PALM[1] approach) shows clear rings and starts resolving the eight corners (Fig. 1m), even when imaged in living cells (Supplementary Fig. 4). The highest resolution is reached using organic dyes (Fig. 1n,o), where the eight corners are very well resolved (Fig. 1n–r). The increasing lateral resolution was
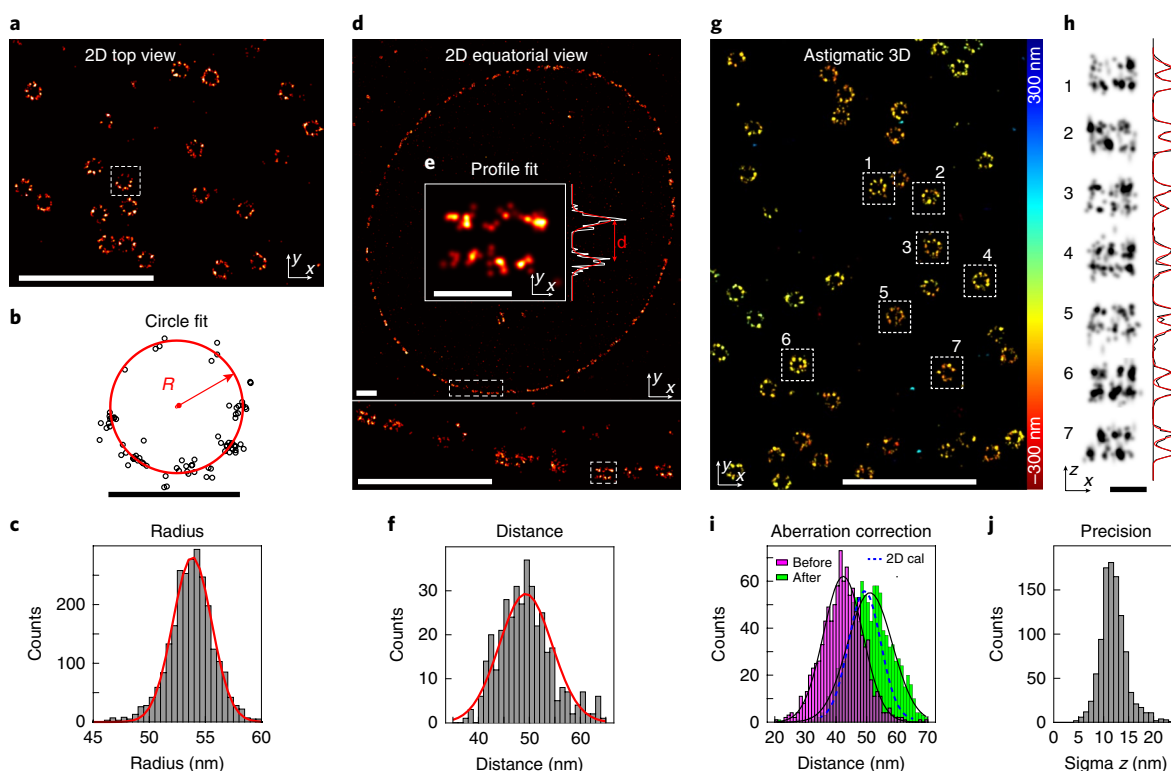
Fig. 2 | Nuclear pores as calibration reference standards. a–h, Experimental characterization of Nup96 positions in the NPC. **a**, SMLM image of lower nuclear envelope. **b**, Circle fit of a single NPC. **c**, Histogram of fitted radii ($R = 53.7 \pm 2.1$ nm, $N = 3$, $n_C = 7$, $n_{NPC} = 2{,}536$). **d**, Equatorial SMLM image of Nup96. **e**, A single NPC in a side view. A fit with a double Gaussian returns the ring distance d and the standard deviation of each ring. **f**, Histogram of separation between rings ($d = 49.3 \pm 5.2$ nm, $N = 2$, $n_C = 14$, $n_{NPC} = 379$). **g**, 3D SMLM image of lower nuclear envelope. The localizations are color-coded according to their z position. **h**, xz reconstructions with z profiles as indicated. **i**, NPCs as calibration reference standard for astigmatic 3D SMLM. Histogram of ring distances before correction (magenta, $d = 42.1 \pm 1.1$ nm, $N = 1$, $n_C = 3$, $n_{NPC} = 1{,}021$) and after correcting for depth-induced calibration errors (green, $d = 49.8 \pm 1.9$ nm). **j**, Standard deviation of z profiles from the double-Gaussian fit result in an upper bound for the experimental localization precision in z of 13.3 ± 1.0 nm ($N = 1$, $n_C = 3$, $n_{NPC} = 1{,}021$). N denotes the number of biologically independent experiments, n_C is the number of imaged cells and n_{NPC} is the number of analyzed NPCs. All values depict weighted mean ± s.d., based on n_{NPC}. Representative images of two (**d,e**) three (**g**) or four (**a**) independent experiments are shown. Scale bars, 1 μm (**a,d,g**) and 100 nm (**b,e,h**). All data on Nup96-SNAP-AF647 in GLOX/MEA.

confirmed in the Fourier spectrum[27] (Supplementary Fig. 3a) and by Fourier ring correlation[28] (Supplementary Fig. 3b). Superresolution approaches with even higher resolution, such as DNA-PAINT, can resolve the four individual proteins in each corner[29].

Our cell lines are also ideal to quantify the axial resolution of 3D superresolution imaging. A sufficient z resolution allows resolving the two rings of the NPC in an axial profile, where the standard deviation of each peak is an upper limit for the experimental localization precision (Figs. 1s and 2h,j).

Microscope calibration. The calibration of a superresolution microscope can be verified by comparing measured distances between Nup96 clusters to the ground truth, which we measured using an automated SMLM microscope with a precisely calibrated pixel size (Methods). The average radius of the NPC was $R = 53.7 \pm 2.1$ nm in Nup96-SNAP cells (Fig. 2a–c, all values are mean ± s.d. unless otherwise noted) and similar in the other cell lines (Supplementary Fig. 5), except for antibody-labeled Nup96-GFP with $R = 64.3 \pm 2.6$ nm. The cytoplasmic and nucleoplasmic rings were 49.3 ± 5.2 nm apart (Fig. 2d–f and Methods) and azimuthally shifted by $8.8° \pm 0.6$ (Fig. 2g,h and Methods).

In addition to the pixel size, our cell lines can be used to verify the axial calibration in 3D SMLM. This is challenging, as aberrations or imperfect point spread function (PSF) models can lead to depth-dependent localization errors, especially when using oil objectives[30]. Moreover, the refractive index difference between oil and the aqueous

sample leads to an image compressed in z. This can be corrected by applying a refractive index mismatch factor (RIMF)[12], which, however, is usually not precisely known and difficult to calibrate.

Here, we used our tagged Nup96 cell lines to validate the z calibration of our astigmatic SMLM microscope by measuring the distance between the two rings in thousands of NPCs in three dimensions. The average distance was $d = 42.1 \pm 1.1$ nm (Fig. 2i, based on a RIMF of 0.8), and thus smaller than the true value of 49.3 nm. Furthermore, the distance between the rings was correlated to the distance between NPC and coverslip (Supplementary Fig. 6a), indicating aberrations. After correcting for these aberration-induced fitting errors with a method we recently developed[30], the z dependence was reduced (Supplementary Fig. 6b) and the average corrected distance is $d = 49.8 \pm 1.9$ nm. Based on these results, we could calibrate the RIMF to be 0.79.

Effective labeling efficiencies. Besides the localization precision, the information content of SMLM images critically depends on how densely the imaged structures are decorated with fluorophores. This can be described by the effective labeling efficiency (ELE), which represents the fraction of target proteins that carry a fluorophore that is detected as a usable localization (that is, brightness above background, fitted with acceptable confidence). By definition, this parameter takes into account conjugation efficiency between dye and ligand, bleaching during initial off-switching and the fraction of nonfunctioning fluorophores.
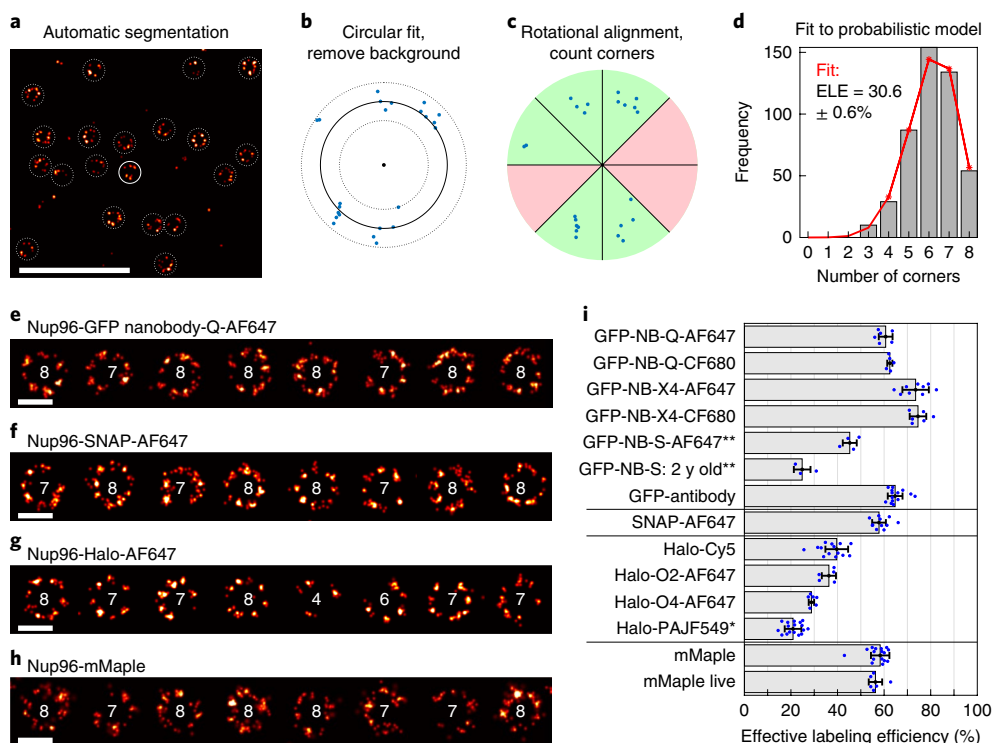
Fig. 3 | Effective labeling efficiencies. a–d, Workflow. **a**, All NPCs in a cell are automatically segmented. **b**, We fit a circle to the localizations and reject localizations outside a ring as background localizations. **c**, We rotate the localizations to optimally fit an eight-fold-symmetric template and count the number of slices that contain at least one localization. **d**, We fit the histogram of the number of corners with a probabilistic model to directly obtain the absolute ELE. The statistical error is estimated by bootstrapping with 20 re-sampled data sets. **e–h**, Gallery of NPCs. **e**, Nup96-GFP labeled with an anti-GFP nanobody coupled to AF647. **f**, Nup96-SNAP labeled with BG-AF647, measured in GLOX/MEA. **g**, Nup96-Halo labeled with chloroalkane-AF647. **h**, Nup96-mMaple. The numbers indicate the numbers of visible corners the algorithm detected. **i**, Effective labeling efficiencies for various cell lines and ligands. Bars denote the mean, error bars the standard deviation and individual data points measurements of a single cell. These data are derived from N biologically independent experiments, n_C imaged cells and n_{NPC} analyzed NPCs: GFP-NB-Q-AF647: $N=2$, $n_C=6$, $n_{NPC}=2{,}913$; GFP-NB-Q-CF680: $N=2$, $n_C=5$, $n_{NPC}=1{,}805$; GFP-NB-X4-AF647: $N=2$, $n_C=9$, $n_{NPC}=4{,}303$; GFP-NB-X4-CF680: $N=2$, $n_C=6$, $n_{NPC}=2{,}011$; GFP-NB-S-AF647: $N=2$, $n_C=4$, $n_{NPC}=8{,}768$; GFP-NB-S-AF647 (2 y): $N=2$, $n_C=3$, $n_{NPC}=1{,}000$; GFP-Antibody: $N=3$, $n_C=14$, $n_{NPC}=7{,}380$; SNAP-AF647: $N=4$, $n_C=11$, $n_{NPC}=5{,}372$; Halo-Cy5: $N=5$, $n_C=14$, $n_{NPC}=5{,}967$; Halo-O2-AF647: $N=2$, $n_C=5$, $n_{NPC}=1{,}393$; Halo-O4-AF647: $N=2$, $n_C=6$, $n_{NPC}=3{,}395$; Halo-PA-JF549: $N=3$, $n_C=17$, $n_{NPC}=4{,}066$; mMaple: $N=6$, $n_C=16$, $n_{NPC}=8{,}146$; mMaple live: $N=3$, $n_C=6$, $n_{NPC}=1{,}343$; Example images for all labels can be found in Supplementary Fig. 9, and imaging conditions are listed in Supplementary Tables 1 and 4. Representative images of two (**e,g**), four (**a,f**) or six (**h**) independent experiments are shown. Scale bars, 1 μm (**a**) and 100 nm (**e–h**). *Labeled in live cells, imaged after fixation. **Measured on Nup107-GFP.

Previously, the maturation efficiency of photo-activatable proteins has been estimated using receptors on the cell surface[14] or by mathematical modeling of fluorophore photophysics[31], and binding efficiencies of anti-GFP antibodies were measured[15]. However, a robust approach to measure the absolute ELE of common labeling strategies inside cells is still missing, limiting a systematic optimization of image quality in SMLM.

Our Nup96 cell lines provide a simple assay to directly measure absolute ELEs. When the ELE is low, NPCs appear as incomplete rings with missing corners. Thus, by statistically analyzing the number of corners of many NPCs, we can infer the absolute ELE. Here, we developed a workflow to automatically determine the number of corners in hundreds of NPCs (Fig. 3 and Methods). The variability of the measured ELE between cells and biological replicates was typically smaller than 10% (s.d., Fig. 3i). Using simulations (Supplementary Fig. 7), we showed that this approach is robust over a large range of ELEs, localization precisions and number of re-activations. Only for very high (>90%) and very low (<10%) ELE the precision is reduced and quantification of low affinity binders might necessitate co-staining with, for example, WGA (wheat germ agglutinin) for unbiased segmentation.

Using this workflow, we systematically compared the ELEs of different anti-GFP nanobodies[32], and SNAP-tag and HaloTag ligands with different organic dyes (Fig. 3i and Supplementary Table 1). Here, we observed the highest ELEs of ~74% using a commercial mixture of two different anti-GFP nanobodies. Other monoclonal commercial anti-GFP nanobodies achieved ~62%, while anti-GFP nanobodies that we generated in the laboratory showed a lower ELE of 45%, which was further reduced to 25% after 2 years of storage in the fridge. Indirect immunofluorescence reached an ELE of 65%.

For Nup96-SNAP labeled with BG-AF647 we achieved an ELE of 58%. Stored SNAP-tag-stained samples were stable over years (shown for Nup107-SNAP in Supplementary Fig. 8) with only minor loss in ELE, facilitating prolonged regular usage of these standard samples.

Using HaloTag, we achieved lower ELEs of 21–40% with four different ligands. While the photo-activatable ligand PA-JF549 (ref. [33]) showed no specific labeling in fixed cells, it could be used for live-cell labeling with an ELE of 21%. We note that, while a single AF647 dye is localized on average 3.4 ± 0.4 times, PA-JF549 produces on average 1.3 ± 0.1 localizations and thus shows little blinking. This is well suited to investigate protein clustering as it reduces false positives caused by re-activation of fluorophores.

Simulations (Supplementary Fig. 7) indicated that our approach of quantifying the ELE works even when the individual corners are not always resolved. Thus, we extended our analysis to the

Table 1 | Imaging conditions

Sample	Buffers	Effective LE (%)	Photons per localization	Localizations per fluorophore	N/cells/NPCs analyzed
SNAP-AF647	35 mM MEA + GLOX	58 ± 3	10,168 ± 982	3.9 ± 0.9	4/11/5,372
	35 mM MEA + GLOX in D_2O	56 ± 3	10,079 ± 423	3.6 ± 0.4	2/5/3,379
	143 mM BME + GLOX	64 ± 4	12,904 ± 689	5.4 ± 0.5	3/8/3,724
	35 mM MEA + 50 mM sodium sulfite	40 ± 2	7,006 ± 513	1.5 ± 0.1	2/5/2,708
mMaple fixed	50 mM Tris in H_2O	55 ± 4	1,169 ± 36	2.5 ± 0.2	2/7/3,126
mMaple fixed	50 mM Tris in D_2O	58 ± 4	1,783 ± 118	2.8 ± 0.2	6/16/8,146
mMaple live	50 mM Tris in D_2O	56 ± 3	1,621 ± 159	2.9 ± 0.1	3/6/1,343

ELE, mean photons per localization and mean localizations per fluorophore for Nup96-SNAP-AF647 and Nup96-mMaple in commonly used imaging buffers. Analysis performed after merging localizations occurring in consecutive frames (Methods). All values are weighted mean ± s.d., based on number of analyzed NPCs. N denotes the number of biologically independent experiments. Example images can be found in Supplementary Fig. 9.

photoconvertible fluorescent protein mMaple. We found an ELE of 58%, indicating that even though 100% of all Nup96 are fused to mMaple, about 40% of them are not detected as a localization. This is likely due to improper folding, insufficient brightness or incomplete photoconversion, in line with previous reports[14,31].

Taken together, this assay provides an easy way for any laboratory using SMLM to monitor the ELEs of their labeling reagents, thus avoiding the use of suboptimal labels.

Imaging conditions. Numerous factors influence image quality in SMLM, including imaging buffers, laser intensities, exposure times, filters and settings in the analysis software. To find optimal conditions, these factors are varied while optimizing various read-outs for quality, including fluorophore brightness, low background, on-times, duty cycle, localization precision, ELE, number of re-activations, imaging speed or stability of imaging buffers. Such optimization requires a robust standard sample with small variability to allow detection of subtle changes.

We used our reference standards to read out these parameters, to compare various common imaging conditions (Table 1 and Supplementary Fig. 9). We confirmed that AF647 shows increased brightness and number of localizations per fluorophore in BME[34] compared to the MEA buffer, reduced brightness and number of localizations per fluorophore in sulfite buffer[35] and no substantial change in D_2O (ref. [36]). We found that a high ELE correlates with a large number of localizations per fluorophore, possibly due to less bleaching during the first switching-off cycle. Finally, we found that paraformaldehyde fixation did not change mMaple photophysics or ELE and confirmed that mMaple becomes brighter in D_2O compared to H_2O (ref. [37]).

Counting proteins. Knowing the stoichiometry of a multi-protein assembly is essential for functional studies. Converting gray values from a fluorescence microscopy image to absolute protein numbers requires careful calibration of the microscope . The Nup96-GFP cell line is well suited to this task, as the majority of nuclear pores are resolved even in diffraction-limited microscopy (Figs. 1f,g and 4a). Thus, we can calibrate precisely how bright 32 GFP-labeled proteins are, and use this calibration to determine the unknown abundance of a different GFP-labeled protein. For validation, we chose Nup107, another nucleoporin present in 32 copies per NPC[38]. In a simple brightness analysis, we evaluated the intensity of the brightest pixel of a local intensity maximum as a measure for the brightness of the NPC and found similar average values for Nup96-GFP and Nup107-GFP[39] (Fig. 4a–d).

SMLM allows counting of proteins in dense structures, but relating the number of localizations to the number of proteins is not trivial. Incomplete labeling leads to undercounting, while repeated fluorophore re-activation induces overcounting. Previous approaches attempted to calibrate blinking and other photophysical properties of fluorophores[40–42], which, however, cannot account for long-lived dark states and incomplete labeling or maturation. Furthermore, a variety of counting references have been developed including self-assembling oligomers[16], DNA-structures[15], receptors[14] or a combination of fluorescent protein oligomers[31,43,44]. While this is a powerful approach, a major limitation is the need for faithful segmentation, which is often strongly dependent on algorithmic parameters. Background localizations or incompletely assembled or labeled reference structures lead to an underestimation of the reference brightness, whereas fusion of double-structures or a cutoff during segmentation and thus loss of small structures leads to an overestimation. Moreover, the detection probability of a fluorophore depends on its z position, which renders cytoplasmic reference structures less accurate.

Our cell lines overcome many of these limitations. NPCs have a characteristic shape and large size, never overlap and are thus easy to segment. They are abundant for improved statistics and are at defined z positions. To validate the use of Nup96-mMaple as a counting reference standard, we generated a stable human embryonic kidney (HEK) 293T cell line where Nup107-mMaple was overexpressed, while endogenous Nup107 was knocked down (Supplementary Fig. 10). We found 32.1 ± 2.5 Nup107 molecules per NPC (Fig. 4e–h), highlighting the consistency of this counting approach.

Accurate counting requires complete tagging of all target proteins, which is laborious in mammalian cells. We thus extended our counting references to *Saccharomyces cerevisiae*, where homologous recombination allows for fast and efficient endogenous labeling (Supplementary Tables 2 and 3). We chose the nucleoporin Nup188 as the reference standard, which is present in 16 copies per NPC[45,46]. We endogenously tagged Nup188 with mMaple in yeast cells that additionally express a GFP-marker for identification. This allowed us to simultaneously image reference and target cells in the same field of view (Fig. 4i,j). We first validated this approach by counting Nup82, which is present also in 16 copies[45,46], and by counting Nup82 and Nup188 molecules together within a strain where both were tagged with mMaple (Fig. 4k,l). The measured copy numbers of 15.7 ± 0.7 and 30.3 ± 1.7 agree well with their expected values of 16 and 32, respectively.

We then counted the nucleoporins Nup192 and Nic96 (Fig. 4m). Nup192 was found in 16.4 ± 1.8 copies per NPC, agreeing with previous reports[45,46]. For Nic96 we found 26.8 ± 1.2 copies when Nic96 was tagged at the C terminus, contradicting previous reports that found 32 copies of Nic96[45]. It was recently proposed that C-terminal

Table 2 | Buffers used in this work

Buffer	Composition	Samples	Reference
Fixation buffer (FB)	2.4% (w/v) formaldehyde in PBS		
Permeabilization buffer (PB)	0.4% (v/v) Triton X-100 in PBS		
Quenching solution (QS)	100 mM NH$_4$Cl in PBS		
Transport buffer (TRB)	20 mM HEPES pH 7.5 110 mM KAc 1 mM EGTA 250 mM sucrose in H$_2$O		Pleiner et al. [51] Göttfert et al.[52]
Transport buffer with BSA (TBA)	1% (w/v) BSA in TRB		Pleiner et al.[51] Göttfert et al.[52]
50 mM Tris in D$_2$O	50 mM Tris/HCl pH 8 in 95% (v/v) D$_2$O	U2OS Nup96-Halo PA-JF549 U2OS Nup96-mMaple HEK Nup107-mMaple Yeast NPC-mMaple	Ong et al.[37]
50 mM Tris in H$_2$O	50 mM Tris/HCl pH 8 in H$_2$O	U2OS Nup96-mMaple	
GLOX/MEA	50 mM Tris/HCl pH 8 10 mM NaCl 10% (w/v) D-glucose 500 µg ml^{-1} glucose oxidase 40 µg ml^{-1} glucose catalase 35 mM MEA in H$_2$O	U2OS Nup96-mEGFP nanobodies U2OS Nup96-mEGFP antibodies[a] U2OS Nup96-Halo O2-AF647 U2OS Nup96-Halo O4-AF647 U2OS Nup96-Halo Cy5 U2OS Nup96-SNAP AF647	Heilemann et al.[53]
GLOX/BME	50 mM Tris/HCl pH 8 10 mM NaCl 10% (w/v) D-glucose 500 µg ml^{-1} glucose oxidase 40 µg ml^{-1} glucose catalase 143 mM BME in H$_2$O	U2OS Nup96-SNAP AF647	Bates et al.[54]
GLOX/MEA in D$_2$O	50 mM Tris/HCl pH 8 10 mM NaCl 10% (w/v) D-glucose 500 µg ml^{-1} Glucose oxidase 40 µg ml^{-1} Glucose catalase 35 mM MEA in 90% (v/v) D$_2$O	U2OS Nup96-SNAP AF647	Klehs et al.[36]
Sulfite/MEA	50 mM Tris/HCl pH 8 50 mM Na$_2$SO$_3$/NaOH pH 8 35 mM MEA in H$_2$O	U2OS Nup96-SNAP AF647	Hartwich et al.[35]

[a]GLOX/MEA with 100 mM MEA instead of 35 mM to decrease the fraction of fluorophores in their on-state to suitable level.

tagging impedes Nic96 function[46], and indeed we measured 33.0 ± 2.0 copies of N-terminally tagged Nic96. When we introduced an additional GFP tag at the C terminus of Nup49, which interacts with the C terminus of Nic96, we again measured only 27.8 ± 1.7 copies even for N-terminally tagged Nic96. Our findings demonstrate the reproducibility of our method, and emphasize the risk of tagging artifacts. Careful quantification of proteins with our counting approach offers an experimental avenue to systematically control for them.

As yeast cells duplicate every ~2 h, maturation times of fluorescent proteins must be considered. Assuming a maturation time of 48 min for mMaple[47] results in 28% of unmatured mMaple in the steady state (Methods). To experimentally test the influence of maturation on our measurements, we stopped protein synthesis by cycloheximide (CHX), reasoning that mMaple synthesized before the treatment should mature to completion. The measured increase in the number of localizations by $11 \pm 6\%$ was lower than estimated above, hinting at a delay in incorporation of Nup188 into the NPC, at degradation of newly synthesized Nup188, at a faster maturation time than previously estimated or at a maturation of mMaple after fixation. Generally, we recommend using this or a related approach to stop protein synthesis whenever the lifetime of the target protein is short or unknown.

Discussion

By homozygously labeling Nup96 with four common tags, we generated reference standards for a variety of important applications in microscopy. Shared together with the software to perform all analyses, the cell lines enable the community to benchmark resolution and calibration of their microscopes, to optimize imaging conditions with high sensitivity, to determine effective labeling efficiencies of their labels and to count protein copy numbers.

The assays presented here are robust and reproducible due to the stereotypic architecture of the NPC. We observed some biological variation in the dimension of the NPC structure (Fig. 2), in line with previous reports by electron microscopy[48]. Thus, a statistical analysis of many NPCs is needed for accurate parameter estimates. This heterogeneity might be interesting with respect to nuclear pore biology, and the data accompanying this manuscript could form the basis for such analysis. Although present, this structural variability is still smaller than that of 3D DNA origami standard samples[10,49]. For some labeling protocols, we observed a cell-to-cell variability of the ELE with a subset of cells showing reduced labeling, stressing the need for replicates and optimal sample preparation. Finally, artifacts (for example, by drift or over-activation) or insufficient localization precision impede accurate determination of ELEs.

Intracellular labeling with SNAP-tag or HaloTag did not result in complete labeling as is possible in vitro[20,21]. We observed that the choice of linker and dye strongly affected the ELE, in line with a recent report[50]. Also, with anti-GFP nanobodies labeling was not complete. Incomplete labeling could arise from incomplete folding of the enzymatic tags, inhibition of the tags by fixatives or intracellular components or by incomplete activation and detection of the fluorophores, imperfect ligands or bleaching during the initial
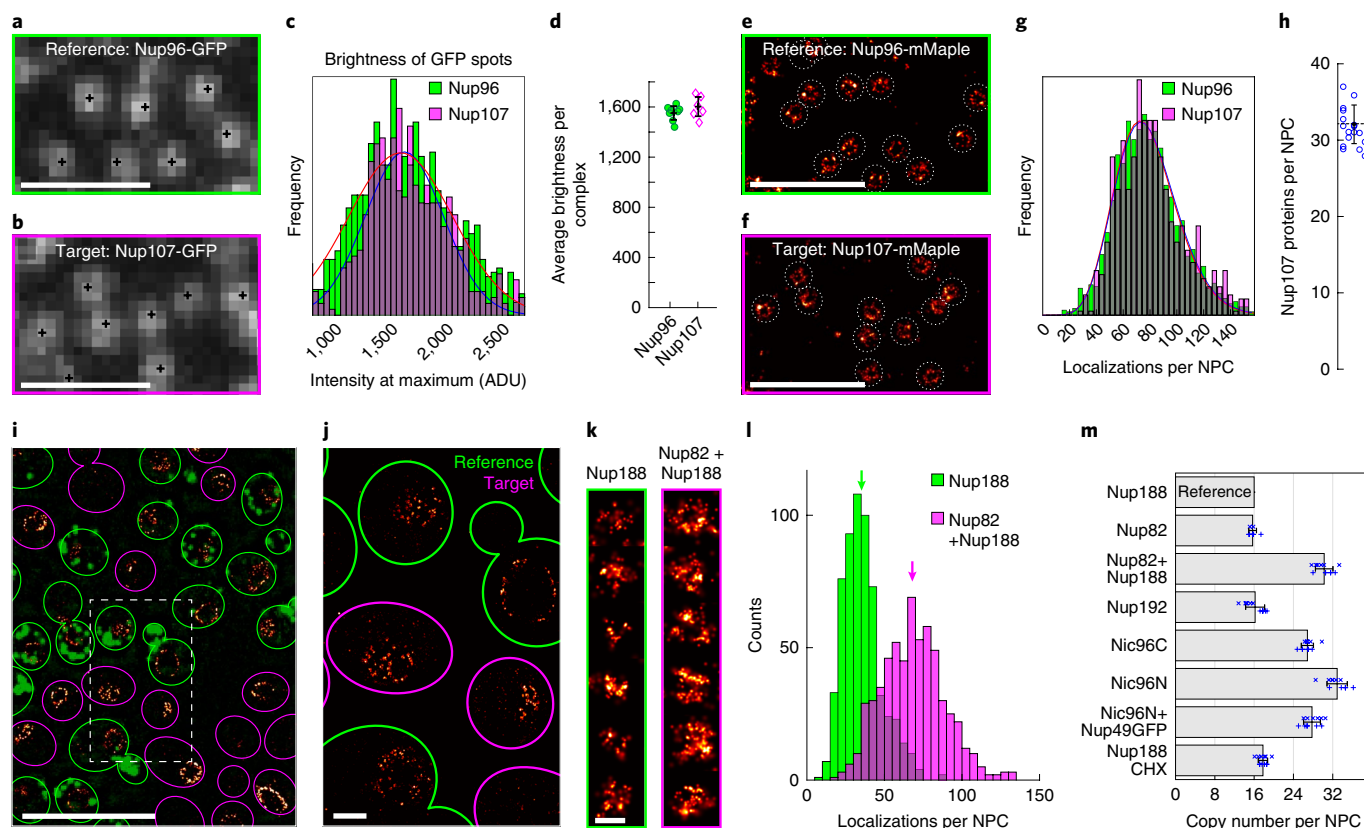
Fig. 4 | Counting of protein copy numbers in complexes. a–d, Counting in diffraction-limited microscopy. **a**, Confocal image of the reference protein Nup96-GFP with the majority of nuclear pores resolved. **b**, Confocal image of the target protein Nup107-GFP imaged with the same microscope settings. **c**, Histograms of intensities of local maxima (see Methods) for the reference and target structures together with Gaussian fit to determine the mean intensity values (in analog digital units, ADU). **d**, Mean intensity values for several reference and target cells. These values show a small variation and are similar for reference ($\langle I_{ref}\rangle = 1{,}552 \pm 55$ ADU, $N=1$, $n_C=8$, $n_R=10{,}104$) and target complex ($\langle I_{tar}\rangle = 1{,}603 \pm 77$ ADU, $N=1$, $n_C=6$, $n_T=7{,}178$). **e–h**, Counting with SMLM: reconstructed superresolution image for reference cell line Nup96-mMaple (**e**) and for target cell line Nup107-mMaple (**f**). NPC structures are automatically segmented to determine the numbers of localizations per NPC. **g**, Histogram of number of localizations per NPC for reference and target. The number of Nup107-mMaple proteins per NPC is calculated from the average relative number of localizations. **h**, The stoichiometry of Nup107 in the NPC ($N_{Nup107} = 32.1 \pm 2.5$, $N=5$, $n_C=13$, $n_T=1{,}928$) shows a high accuracy and low statistical errors of this counting approach. **i–m**, Counting in yeast. **i**, Mixture of Nup188-mMaple+Abp1-GFP reference cell lines with Nup82-mMaple+Nup188-mMaple target cell lines, which can be distinguished by the GFP signal. **j,k**, Superresolution reconstruction (**j**) and individual nuclear pores (**k**). **l**, Histograms of the number of localizations per nuclear pore, arrows indicate the mean ($N=2$, $n_C=508$, $n_{NPC}=1{,}190$ for Nup188 and $n_{NPC}=1{,}176$ for Nup82+Nup188). **m**, Copy number of several yeast nucleoporins per NPC, determined using Nup188 as a reference. These data are derived from: Nup82: $N=2$, $n_C=242$, $n_T=678$, $n_R=686$; Nup82+Nup188: $N=2$, $n_C=508$, $n_T=1{,}176$, $n_R=1{,}190$; Nup192: $N=2$, $n_C=558$, $n_T=992$, $n_R=916$; Nic96C: $N=2$, $n_C=304$, $n_T=1{,}102$, $n_R=1{,}127$; Nic96N: $N=2$, $n_C=532$, $n_T=1{,}078$, $n_R=1{,}079$; Nic96N+Nup49GFP: $N=2$, $n_C=303$, $n_T=1{,}137$, $n_R=1{,}149$; Nup188 (CHX treatment): $N=2$, $n_C=521$, $n_T=1{,}157$, $n_R=1{,}154$. N denotes the number of biologically independent experiments, n_C the number of analyzed cells, and n_T/n_R the number of analyzed NPCs for the counting target/reference. Bars denote the mean, error bars the standard deviation and data points individual acquisitions. Shown values depict weighted mean $\pm$ s.d., based on n_{NPC}. Representative images of one (**b**), two (**a,i–k**), five (**f**) or six (**e**) independent experiments are shown. Scale bars, 10 µm (**i**), 1 µm (**a,b,e,f,j**), 100 nm (**k**).

off-switching step in SMLM, which warrants further investigation and optimization.

It should be stressed that the ELE measured on NPCs is not necessarily equal to ELEs on other target proteins due to differences in epitope accessibility and local environment. However, we expect that imaging protocols optimized on Nup96 cell lines will be suitable for other structures, and that labels that achieve only a low ELE on Nup96 will also perform poorly on other targets.

As counting reference standards, NPCs are advantageous to small and globular structures due to the ease of segmentation and their defined z positions. However, some fundamental limitations still apply to any reference-based approach: both target and reference structures need to be in focus and well segmented to exclude overlapping structures and background localizations from outside the imaging plane, and all target proteins need to carry a label, thus

requiring endogenous protein tagging. Furthermore, incomplete maturation of photoconvertible proteins has been reported before[14]. Thus, protein turnover and maturation rates in the cell need to be accounted for, and protein synthesis might need to be stopped for a limited time to ensure all labels are matured. Finally, counting with fluorescent proteins, as we have used here, is preferable to counting with external labels, where different epitope accessibilities of the tags between reference and target need to be considered.

Our Nup96 cell lines optimally complement the current standard sample for SMLM, that is, immunolabeled microtubules, as they have a defined stoichiometry and 3D arrangement of the fluorophores and are compatible with most common labeling approaches. Together with the community, we will extend the collection of Nup96 cell lines to other fluorescent proteins and peptide tags. We expect that they will find widespread use in many laboratories for

optimization, quality control and counting and that they become the gold standard to quantify effective labeling efficiencies of new dyes and labels.

Online content

Any methods, additional references, Nature Research reporting summaries, source data, statements of code and data availability and associated accession codes are available at https://doi.org/10.1038/s41592-019-0574-9.

References

1. Betzig, E. et al. Imaging intracellular fluorescent proteins at nanometer resolution. *Science* **313**, 1642–1645 (2006).
2. Rust, M. J., Bates, M. & Zhuang, X. Sub-diffraction-limit imaging by stochastic optical reconstruction microscopy (STORM). *Nat. Methods* **3**, 793–795 (2006).
3. Xu, K., Zhong, G. & Zhuang, X. Actin, spectrin, and associated proteins form a periodic cytoskeletal structure in axons. *Science* **339**, 452–456 (2013).
4. Mund, M. et al. Systematic nanoscale analysis of endocytosis links efficient vesicle formation to patterned actin nucleation. *Cell* **174**, 884–896.e17 (2018).
5. Szymborska, A. et al. Nuclear pore scaffold structure analyzed by super-resolution microscopy and particle averaging. *Science* **341**, 655–658 (2013).
6. Ball, G. et al. SIMcheck: a toolbox for successful super-resolution structured illumination microscopy. *Sci. Rep.* **5**, 15915 (2015).
7. Culley, S. et al. Quantitative mapping and minimization of super-resolution optical imaging artifacts. *Nat. Methods* **15**, 263–266 (2018).
8. Sage, D. et al. Super-resolution fight club: assessment of 2D and 3D single-molecule localization microscopy software. *Nat. Methods* **16**, 387–395 (2019).
9. Steinhauer, C., Jungmann, R., Sobey, T. L., Simmel, F. C. & Tinnefeld, P. DNA origami as a nanoscopic ruler for super-resolution microscopy. *Angew. Chem. Int. Ed.* **48**, 8870–8873 (2009).
10. Iinuma, R. et al. Polyhedra self-assembled from DNA tripods and characterized with 3D DNA-PAINT. *Science* **344**, 65–69 (2014).
11. Huang, B., Jones, S. A., Brandenburg, B. & Zhuang, X. Whole-cell 3D STORM reveals interactions between cellular structures with nanometer-scale resolution. *Nat. Methods* **5**, 1047–1052 (2008).
12. Huang, B., Wang, W., Bates, M. & Zhuang, X. Three-dimensional super-resolution imaging by stochastic optical reconstruction microscopy. *Science* **319**, 810–813 (2008).
13. von Appen, A. et al. In situ structural analysis of the human nuclear pore complex. *Nature* **526**, 140–143 (2015).
14. Durisic, N., Laparra-Cuervo, L., Sandoval Álvarez, Á., Borbely, J. S. & Lakadamyali, M. Single-molecule evaluation of fluorescent protein photoactivation efficiency using an in vivo nanotemplate. *Nat. Methods* **11**, 156–162 (2014).
15. Zanacchi, F. C. et al. A DNA origami platform for quantifying protein copy number in super-resolution. *Nat. Methods* **14**, 789–792 (2017).
16. Finan, K., Raulf, A. & Heilemann, M. A set of homo-oligomeric standards allows accurate protein counting. *Angew. Chem. Int. Ed.* **54**, 12049–12052 (2015).
17. Zanacchi, F. C., Manzo, C., Magrassi, R., Derr, N. D. & Lakadamyali, M. Quantifying protein copy number in super-resolution using an imaging-invariant calibration. *Biophys. J.* **116**, 2195–2203 (2019).
18. Löschberger, A. et al. Super-resolution imaging visualizes the eightfold symmetry of gp210 proteins around the nuclear pore complex and resolves the central channel with nanometer resolution. *J. Cell Sci.* **125**, 570–575 (2012).
19. McEvoy, A. L. et al. mMaple: a photoconvertible fluorescent protein for use in multiple imaging modalities. *PLoS ONE* **7**, e51314 (2012).
20. Keppler, A., Pick, H., Arrivoli, C., Vogel, H. & Johnsson, K. Labeling of fusion proteins with synthetic fluorophores in live cells. *Proc. Natl Acad. Sci. USA* **101**, 9955–9959 (2004).
21. Los, G. V. et al. HaloTag: a novel protein labeling technology for cell imaging and protein analysis. *ACS Chem. Biol.* **3**, 373–382 (2008).
22. Klar, T. A., Jakobs, S., Dyba, M., Egner, A. & Hell, S. W. Fluorescence microscopy with diffraction resolution barrier broken by stimulated emission. *Proc. Natl Acad. Sci. USA* **97**, 8206–8210 (2000).
23. Chen, F., Tillberg, P. W. & Boyden, E. S. Expansion microscopy. *Science* **347**, 543–548 (2015).
24. Gustafsson, N. et al. Fast live-cell conventional fluorophore nanoscopy with ImageJ through super-resolution radial fluctuations. *Nat. Commun.* **7**, 12471 (2016).
25. Pesce, L., Cozzolino, M., Lanzanò, L., Diaspro, A. & Bianchini, P. Measuring expansion from macro- to nanoscale using NPC as intrinsic reporter. *J. Biophotonics* **12**, e201900018 (2019).
26. Gambarotto, D. et al. Imaging cellular ultrastructures using expansion microscopy (U-ExM). *Nat. Methods* **16**, 71 (2019).
27. Demmerle, J., Wegel, E., Schermelleh, L. & Dobbie, I. M. Assessing resolution in super-resolution imaging. *Methods* **88**, 3–10 (2015).
28. Nieuwenhuizen, R. P. J. et al. Measuring image resolution in optical nanoscopy. *Nat. Methods* **10**, 557–562 (2013).
29. Schlichthaerle, T. et al. Direct visualization of single nuclear pore complex proteins using genetically-encoded probes for DNA-PAINT. *Angew. Chem. Int. Ed.* **58**, 13004–13008 (2019).
30. Li, Y., Wu, Y.-L., Hoess, P., Mund, M. & Ries, J. Depth-dependent PSF calibration and aberration correction for 3D single-molecule localization. *Biomed. Opt. Express* **10**, 2708–2718 (2019).
31. Fricke, F., Beaudouin, J., Eils, R. & Heilemann, M. One, two or three? Probing the stoichiometry of membrane proteins by single-molecule localization microscopy. *Sci. Rep.* **5**, 14072 (2015).
32. Ries, J., Kaplan, C., Platonova, E., Eghlidi, H. & Ewers, H. A simple, versatile method for GFP-based super-resolution microscopy via nanobodies. *Nat. Methods* **9**, 582–584 (2012).
33. Grimm, J. B. et al. Bright photoactivatable fluorophores for single-molecule imaging. *Nat. Methods* **13**, 985–988 (2016).
34. Dempsey, G. T., Vaughan, J. C., Chen, K. H., Bates, M. & Zhuang, X. Evaluation of fluorophores for optimal performance in localization-based super-resolution imaging. *Nat. Methods* **8**, 1027–1036 (2011).
35. Hartwich, T. M. et al. A stable, high refractive index, switching buffer for super-resolution imaging. Preprint at *bioRxiv* https://doi.org/10.1101/465492 (2018).
36. Klehs, K. et al. Increasing the brightness of cyanine fluorophores for single-molecule and superresolution imaging. *Chem. Phys. Chem.* **15**, 637–641 (2014).
37. Ong, W. Q., Citron, Y. R., Schnitzbauer, J., Kamiyama, D. & Huang, B. Heavy water: a simple solution to increasing the brightness of fluorescent proteins in super-resolution imaging. *Chem. Commun.* **51**, 13451–13453 (2015).
38. Ori, A. et al. Cell type-specific nuclear pores: a case in point for context-dependent stoichiometry of molecular machines. *Mol. Syst. Biol.* **9**, 648–648 (2013).
39. Otsuka, S. et al. Nuclear pore assembly proceeds by an inside-out extrusion of the nuclear envelope. *eLife* **5**, e19071 (2016).
40. Annibale, P., Vanni, S., Scarselli, M., Rothlisberger, U. & Radenovic, A. Quantitative photo activated localization microscopy: unraveling the effects of photoblinking. *PLoS ONE* **6**, e22678 (2011).
41. Lee, S.-H., Shin, J. Y., Lee, A. & Bustamante, C. Counting single photoactivatable fluorescent molecules by photoactivated localization microscopy (PALM). *Proc. Natl Acad. Sci. USA* **109**, 17436–17441 (2012).
42. Rollins, G. C., Shin, J. Y., Bustamante, C. & Pressé, S. Stochastic approach to the molecular counting problem in superresolution microscopy. *Proc. Natl Acad. Sci. USA* **112**, E110–E118 (2014).
43. Puchner, E. M., Walter, J. M., Kasper, R., Huang, B. & Lim, W. A. Counting molecules in single organelles with superresolution microscopy allows tracking of the endosome maturation trajectory. *Proc. Natl Acad. Sci. USA* **110**, 16015–16020 (2013).
44. Baldering, T. N. et al. Synthetic and genetic dimers as quantification ruler for single-molecule counting with PALM. *Mol. Biol. Cell* **30**, 1369–1376 (2019).
45. Kim, S. J. et al. Integrative structure and functional anatomy of a nuclear pore complex. *Nature* **555**, 475–482 (2018).
46. Rajoo, S., Vallotton, P., Onischenko, E. & Weis, K. Stoichiometry and compositional plasticity of the yeast nuclear pore complex revealed by quantitative fluorescence microscopy. *Proc. Natl Acad. Sci. USA* **115**, E3969–E3977 (2018).
47. Wang, S., Moffitt, J. R., Dempsey, G. T., Xie, X. S. & Zhuang, X. Characterization and development of photoactivatable fluorescent proteins for single-molecule-based superresolution imaging. *Proc. Natl Acad. Sci. USA* **111**, 8452–8457 (2014).
48. Beck, M., Lučić, V., Förster, F., Baumeister, W. & Medalia, O. Snapshots of nuclear pore complexes in action captured by cryo-electron tomography. *Nature* **449**, 611–615 (2007).
49. Deschamps, J., Mund, M. & Ries, J. 3D superresolution microscopy by supercritical angle detection. *Opt. Express* **22**, 29081–29091 (2014).
50. Erdmann, R. S. et al. Labeling strategies matter for super-resolution microscopy: a comparison between halotags and SNAP-tags. *Cell Chem. Biol.* **26**, 584–592 (2019).

Author contributions

J.R. conceived the approach. B.N., M.Ku., V.J.S., J.E., J.V.T. and U.M. generated the cell lines. J.V.T., M.Ka., K.C., P.H., S.K.P., M.R., D.H., K.C.K., S.J.H., Y.L., Y.W., M.M., U.M. and J.R. developed the methods, wrote the software, acquired and analyzed the data. R.H. and P.M.P. acquired the expansion microscopy data. J.V.T., M.Ka., P.H., M.M. and J.R. wrote the manuscript with input from all authors.

Competing interests

The authors declare no competing interests.

Additional information

Supplementary information is available for this paper at https://doi.org/10.1038/s41592-019-0574-9.

Correspondence and requests for materials should be addressed to J.R.

Peer review information Rita Strack was the primary editor on this article and managed its editorial process and peer review in collaboration with the rest of the editorial team.

Reprints and permissions information is available at www.nature.com/reprints.

Publisher's note Springer Nature remains neutral with regard to jurisdictional claims in published maps and institutional affiliations.

Methods

Generation of CRISPR cell lines. All cell lines are distributed by Cell Line Services (CLS, clsgmbh.de, Nup96-SNAP no. 300444, Nup96-Halo no. 300448, Nup96-mEGFP no. 300174 and Nup96-mMaple no. 300461).

Genome editing was performed using CRISPR-Cas9D10A nickase as described in Koch et al.[55]. The genomic RNA sequences for Nup96 C terminus are as follows, sense: 5′-GTTGGGAGCCTGTGAGCCCC-3′ and antisense: 5′-CAGTTCTCGCAGATAGGACT-3′.

The synthetic gene pNup96-mEGFP donor plasmid encoding for left (1.1 kb) and right (0.8 kb) homology arms for the C terminus of Nup96 was assembled from synthetic oligonucleotides and/or PCR products. A linker sequence (5′ ACTAGTCGACGGTACCGCGGGCCCGGGATCCACCGGCCGGTCGCCACC 3′) between the left homology arm containing multiple cloning sites was inserted to aid the generation of donor plasmids encoding for other tags. The fragment was inserted into the pMA-RQ (ampR) vector backbone.

Donor plasmids encoding for mMaple[19], SNAP$_f$ tag[56] (NEB) and HaloTag (Promega) were generated by swapping out mEGFP using restriction enzymes *EagI-HF* and *NheI-HF* (NEB). Tag-sequences can be found in the Supplementary Information.

Southern blotting of Nup96. Southern blotting was performed in accordance to Koch et al.[55]. Genomic DNA was prepared using the Wizard Genomic DNA Purification kit (Promega) and digested with *SspI-HF* and *MfeI-HF* (NEB). The probe sequences used are as follows:

Nup96 C terminus:
(5′-TCCAGTTTCTCTCTGCCACATCCACCTGTTTAAATTATCTACAT-GGCTTGTGATTTTCAGGATTTATTACTGTTTTGTGTTTTCTTATTTA-TTTTCTATCAGTTTCATGAGAGCAAATAACCTGTCTTGCTCTTGATCCTCC TGCCCCCTGCACACAGCTTTTTTGGTGTTTTAGAAAAGGCTATAAACTTG GAGTCAGGGGACCT-3′);

mEGFP: (5′-CACATGAAGCAGCACGACTTCTTCAAGTCCGCCATGCC-CGAAGGCTACGTCCAGGAGCGCACCATCTTCTTCAAGGACGACGGCAA-CTACAAGACCCGCGCCGAGGTGAAGTTCGAGGGCGACACCCTGGTG-AACCGCATCGAGCTGAAGGGCATCGACTTCAAGGAGGACGGCAACATC-CTGGGGCACAAGCTGGAGTACAACTACAACAGCCACAACGTCTATATCA TGGCCGACAAGCAGAAGAACGGCATCAAGGTGAACTTCAAGATCCGCC ACAACATCGAGGACGGCAGCGTGCAGCTCGCCGACCACTACCAGCAGA ACACCC-3′);

mMaple: (5′-AGCATGACCTACGAGGACGGCGGCATCT-GCATCGCCACCAACGACATCACAATGGAGGAGGACAGCTT-CATCAACAAGATCCACTTCAAGGGCACGAACTT-3′);

SNAP-tag:
(5′-AAAGACTGCGAAATGAAGCGCACCACCCTGGATAGC-CCTCTGGGCAAGCTGGAACTGTCTGGGTGCGAACAGGGCC-TGCACCGTATCATCTTCCTGGGCAAAGGAACATCT-3′);

HaloTag:
(5′-TGCATTGCTCCAGACCTGATCGGTATGGGCAAATCCGACAAACCA GACCTGGGTTATTTCTTCGACGACCACGTCCGCTTCATGGATGCCTTCA TCGAAGC-3′)

Small interfering RNA silencing of Nup96 in U2OS. To test specificity of the anti-Nup98 antibody, U2OS cells were seeded onto a 35 mm cell culture dish. Then, 48 h after seeding, MISSION esiRNA Human Nup98 (esirna1) (Sigma, EHU087381-20ug, Lot BEV) was introduced using lipofectamine 2000 (Life Technologies). Following that, 48 h after transfection, the cell layer was scraped and cell lysate was collected for western blot analysis.

Western blotting of Nup96. U2OS cell lysates were collected in Pierce RIPA buffer (catalog no. 89900, lot no. NF170965; ThermoFisher Scientific) supplemented with Complete protease inhibitors (Roche) and phenylmethanesulfonylfluoride (PMSF). Cell lysate protein concentration was determined using Pierce BCA protein assay kit (cataolog no. 23225, lot no. QI223168; ThermoFisher Scientific). Then, 50 µg of cell lysate was loaded onto a 4–12% gradient gel and ran at 165 V constant for 45–60 min in 1× MOPS-SDS buffer (NuPAGE) at room temperature (RT). Proteins were then transferred to a PVDF membrane at 15 V constant for 60 min in cold 1× transfer buffer supplemented with 10% (v/v) methanol (Bolt) at RT. Membranes were then blocked in 10% (w/v) milk in TBS-T pH 7.6 for 1 h at RT. After blocking, membranes were incubated in 1:2,000 diluted primary antibody (pAb anti-Nup98, catalog no. NB1000-93325, LotA1, Novus) in 3% (w/v) BSA in TBS-T at 4 °C overnight. Membranes were then incubated in 1:10,000 diluted secondary antibody in 5% (w/v) milk in TBS-T for 1 h at RT. Chemiluminescence reagents were added to the membrane with subsequent film exposure.

Sample preparation. *Buffers.* See Table 2 for a list of the buffers used in this work.

Sample seeding. Before seeding of cells, high-precision 24 mm round glass coverslips (No. 1.5H, catalog no. 117640, Marienfeld) were cleaned by placing them overnight in a methanol:hydrochlorid acid (50:50) mixture while stirring. Following that, the coverslips were repeatedly rinsed with water until they reached

a neutral pH. They were then placed overnight into a laminar flow cell culture hood to dry them before finalizing the cleaning of coverslips by ultraviolet irradiation for 30 min.

For superresolution microscopy, homozygous endogenously tagged cells were seeded on clean glass coverslips 2 d before fixation in such a way that they reach a confluency of about 50–70% on the day of fixation. For diffraction-limited techniques, cells were seeded on 35 mm cell culture dishes with a 10 mm glass bottom insert (catalog no. 627860, Greiner Bio-One) instead. Cells were grown on the coverslip or the 35 mm cell culture dish in growth medium (DMEM (Gibco, no. 11880-02) containing 1× MEM NEAA (catalog no. 11140-035, Gibco), 1× GlutaMAX (catalog no. 35050-038, Gibco) and 10% (v/v) fetal bovine serum (catalog no. 10270-106, Gibco)) for approximately 2 d at 37 °C and 5% CO$_2$. Before further processing, the growth medium was aspirated, and samples were rinsed twice with PBS to remove dead cells and debris. Unless otherwise stated, all experiment replicates were performed on cells of different passage seeded on coverslips. On each coverslip, multiple cells were imaged.

Expansion microscopy (proExM). Expansion of samples was performed as described elsewhere[57]. Briefly, monomer solution (1× PBS, 2 M NaCl, 8.625% (w/w, Sigma) sodium acrylate, 2.5% (w/w, Sigma) acrylamide, 0.15% (w/w, Sigma) N,N′-methylenebisacrylamide) was mixed and cooled to 4 °C before use. Ammonium persulfate (APS, BioRad) initiator and tetramethylethylenediamine (TEMED, Sigma) accelerator were added to the monomer solution up to 0.2% (w/w) each. Samples on coverslips were incubated with the monomer solution plus APS/TEMED in a humidified 37 °C incubator for 1 h for gelation. Proteinase K (New England Biolabs) was diluted 1:100 to 8 units per ml in digestion buffer (50 mM Tris/HCl pH 8, 1 mM EDTA, 0.5% (v/v) Triton X-100, 1 M NaCl, Sigma) and incubated with the gels fully immersed in proteinase solution overnight at 23 °C. Digested gels were next placed in excess volumes of double deionized water for 3–4 h to expand (water changed every 30 min), until the size of the expanding sample plateaued. A small piece of the expanded sample was mounted in an ATTOFLUOR chamber (ThermoFisher Scientific) on 18 mm PLL (Sigma) coated coverslips (Marienfeld) and covered with low-melting agarose (Sigma). To determine the level of sample expansion, the average size of nuclei pre- and post-expansion was measured.

Nanobody labeling of Nup96-mEGFP fusion proteins. U2OS-Nup96-mEGFP cells, either prepared on glass coverslips for superresolution measurements or 35 mm cell culture dishes for diffraction-limited techniques, were stained according to a protocol previously described by Pleiner and colleagues[51]. For this, samples were prefixed for 30 s in transport buffer (TRB) containing 2.4% (w/v) formaldehyde (FA), followed by washing twice in TRB for 5 min each. Plasma membrane-specific permeabilization was achieved by 8 min incubation on ice in TRB containing 25 µg ml^{-1} digitonin (catalog no. D141, Sigma Aldrich). Samples were washed twice for 5 min in TBA. The first round of staining was achieved by incubating the samples upside-down in a drop of TBA containing 100 nM of anti-GFP nanobodies (NanoTag Biotechnologies, FluoTag-Q (catalog no. N0301) or FluoTag-X4 (catalog no. N0304), conjugated to AF647, CF680 or STAR 635P) for 30 min on ice. Residual nanobodies were rinsed away in TBA twice for 5 min each before cells were further fixed in TBA containing 3% (w/v) FA for 10 min followed by two additional washing steps in TBA for 5 min each. Permeabilization of the nuclear envelope was facilitated by 3 min incubation in PB. Samples were washed twice in PBS for 5 min each before exposing them again upside down onto a drop of anti-GFP nanobodies (50 nM in TBA, same nanobodies as in the first round of staining) for 30 min on ice. Finally, weakly and unbound nanobodies were rinsed off in PBS twice for 15 min. For STED-imaging, FluoTag-X4-STAR 635P stained samples were mounted upside down on glass microscopy slides (ThermoFisher Scientific) using Mowiol (Calbiochem). Edges were further sealed with nail polish and then dried overnight at RT.

Indirect immunostaining of Nup96-mEGFP fusion proteins. To fix U2OS-Nup96-mEGFP cells on the glass coverslips, cells were prefixed in FB for 30 s before incubating them 3 min in 0.1% Triton X-100 in PBS and washing twice for 5 min each in PBS. Fixation was completed in FB for 20 min. Samples were quenched for 5 min in QS and then washed twice in PBS for 5 min each. Fixed cells were then further permeabilized using 0.2% Triton X-100 in PBS for 10 min, followed by two more washing steps in PBS for 5 min each before blocking in 2% (w/v) BSA in PBS for 1 h. Binding of primary rabbit anti-GFP antibodies (catalog no. 598, MBL International) to Nup96-GFP fusion proteins was achieved by placing the coverslips upside down onto a drop of primary antibody solution (diluted 1:250 in PBS containing 2% (w/v) BSA) at 4 °C and leaving overnight. Weakly and unbound primary antibodies were subsequently rinsed away with three washing steps in PBS for 5 min each. Secondary antibody labeling was achieved by placing the samples upside-down onto a drop of anti-rabbit antibodies with conjugated AF647 dye (custom made, diluted 1:300 in PBS containing 2% (w/v) BSA) for 1 h at RT. Residual secondary antibody was removed by washing three times with PBS for 5 min.

HaloTag labeling of fixed cells. U2OS-Nup96-Halo cells were stained on previously prepared coverslips using a slightly modified version of the nanobody labeling

protocol described above[51]. Instead of staining the samples in two separate rounds of nanobodies (100 nM in round 1 and 50 nM in round 2), the samples were incubated in HaloTag dye buffer (5 µM of Cy5-HaloTag-ligand (Lavis Lab, HHMI Janelia Research campus) or HaloTag-ligand-O2-AF647/HaloTag-ligand-O4-AF647 (custom substrates from Peps4LS) in TBA) for 1 h at RT in both incubation steps. All other steps were performed in accordance to the above described protocol.

HaloTag live labeling. Coverslips covered in an approximately 50–70% confluent layer of U2OS-Nup96-Halo were incubated in pre-warmed growth medium containing PA-JF549-HaloTag ligand (250–5,000 nM were tested without apparent difference in labeling efficiency; Lavis Lab, HHMI Janelia Research campus) at 37 °C and 5% CO_2 for 1 h. The samples were subsequently rinsed three times in pre-warmed PBS and incubated in pre-warmed growth medium without dye for 1 h at 37 °C and 5% CO_2 to wash off noncovalently bound dye. Following that, the samples were rinsed three times in PBS before prefixing them at RT for 30 s in FB. Permeabilization was facilitated in PB for 3 min before completing the fixation process for 30 min in FB. Subsequently, FA was quenched by incubating the coverslip for 5 min in QS. Sample preparation was finalized by washing twice in PBS for 5 min each.

SNAP-tag labeling of fixed cells. U2OS-Nup96-SNAP cells were prefixed for 30 s in FB before permeabilization in PB for 3 min. To complete fixation, samples were incubated for 30 min in FB. FA was subsequently quenched in QS for 5 min before washing the coverslip twice for 5 min in PBS. To reduce unspecific binding, the sample was incubated for 30 min with Image-iT FX Signal Enhancer (ThermoFisher Scientific) before staining in SNAP dye buffer (1 µM BG-AF647 (New England Biolabs, no. S9136S), 1 µM dithiothreitol, in 0.5% (w/v) BSA in PBS) for 2 h at RT. To remove unbound dye, coverslips were washed three times in PBS for 5 min each.

Fixation of mMaple tagged cell lines. Glass coverslips prepared with U2OS-Nup96-mMaple or HEK-Nup107-mMaple cells were prefixed for 30 s in FB before incubation in PB for 3 min. To complete fixation, samples were incubated for 30 min in FB. FA was subsequently quenched in QS for 5 min before washing the coverslip twice for 5 min in PBS.

Strain and sample preparation for yeast. For protein counting in *S. cerevisiae*, the respective proteins (Nup188, Nup82, Nup192, Nic96, Nup49 and Abp1) were endogenously tagged on the C terminus by homologous recombination. Briefly, we constructed plasmids encoding mMaple and different selectable markers by standard molecular biology methods[58]. The cassette containing a peptide linker, mMaple and the selectable marker was amplified by PCR and transformed into competent yeast cells. Yeast cells were plated on selective plates, grown for 2–3 d until single colonies were obtained. Correct tagging was confirmed by colony PCR and imaging.

N-terminal labeling of Nic96 was performed seamlessly[59]. First, a cassette was amplified by PCR from a vector that contains the first 180 bp of mMaple, the selectable marker for the expression of the URA3 gene and a promoter for the tagged gene of interest surrounded by two I-*SceI* restriction sites and full-length mMaple. This cassette was transformed into yeast cells that express I-*SceI* under control of a galactose inducible promotor. After correct integration was confirmed by colony PCR, the strain was cultivated on plates containing galactose to induce the expression of I-*SceI* and resistance cassette loopout. Successful excision was counterselected on plates containing 5-fluoroorotic acid.

For immobilization of yeast, the coverslips were coated with concanavalin A (ConA, catalog no. C2010, Sigma Aldrich). For this, the coverslips were cleaned overnight in a 1:1 mixture of methanol and hydrochloric acid, washed three times with dH_2O and plasma-cleaned. Next, 20 µl of 4 mg ml⁻¹ ConA in PBS was pipetted onto the coverslip and spread, incubated under a humidified atmosphere for 30 min and then dried.

For superresolution imaging, the respective strains were grown at 30 °C shaking at 220 r.p.m. in synthetic complete medium without tryptophan (SC-Trp) to reduce autofluorescence. A 4 ml overnight culture was inoculated from a single colony on a freshly restreaked plate. In the morning of the experiment, the culture was diluted to an optical density (OD_{600}) of 0.25 in 10 ml of SC-Trp medium and cultured for approximately three more hours to logarithmic phase. To inhibit protein synthesis, CHX was added to a final concentration of 250 µg ml⁻¹ (from a 50 mg ml⁻¹ stock solution) for the last hour of growth. Then, cells from the reference strain (Nup188-mMaple Abp1-mEGFP) and the respective target strain were mixed in a 1:1 ratio and spun down in a table top centrifuge (3 min at 1,000g and RT), resuspended in about 200 µl of residual medium and pipetted onto a ConA-coated coverslip. All subsequent steps were carried out in the dark to prevent pre-conversion of mMaple. After allowing the cells to settle for 20 min, the coverslips were fixed in fixation solution (4% (w/v) FA, 2% (w/v) sucrose, in PBS) for 15 min. Subsequently, remaining FA was quenched by washing twice for 5 min in QS. After washing three times with PBS for 5 min each, the coverslip was ready for imaging.

Microscopy. *Microscope setup and imaging.* All SMLM data were acquired on a custom built widefield setup described previously[4,60]. Briefly, the free output of a commercial laser box (LightHub, Omicron-Laserage Laserprodukte) equipped with Luxx 405, 488 and 638 and Cobolt 561 lasers and an additional 640 nm booster laser (iBeam Smart, Toptica) were collimated and focused onto a speckle reducer (catalog no. LSR-3005-17S-VIS, Optotune, Dietikon) before being coupled into a multi-mode fiber (catalog no. M105L02S-A, Thorlabs). The output of the fiber was magnified by an achromatic lens and focused into the sample to homogeneously illuminate an area of about 1,000 µm². Alternatively, a single-mode fiber (Omicron, LightHUB) could be plugged into the output of the laserbox to allow TIRF imaging. The laser is guided through a laser cleanup filter (390/482/563/640 HC Quad, AHF) to remove fluorescence generated by the fiber. Emitted fluorescence was collected through a high numerical aperture (NA) oil immersion objective (HCX PL APO 160×/1.43 NA, Leica), filtered by a bandpass filter (525/50 (catalog no. FF03-525/50-25, Semrock) for mEGFP; 600/60 (catalog no. NC458462, Chroma) for mMaple and PA-JF549 and 700/100 (catalog no. ET700/100m, Chroma) for AF647, Cy5 and CF680) and imaged onto an Evolve512D EMCCD camera (Photometrics). The z focus was stabilized by an infrared laser that was totally internally reflected off the coverslip onto a quadrant photodiode, which was coupled into closed-loop feedback with the piezo objective positioner (Physik Instrumente). Laser control, focus stabilization and movement of filters was performed using a field-programmable gate array (Mojo, Embedded Micro). The pulse length of the 405 nm (laser intensity 27.5 W cm⁻²) laser is controlled by a feedback algorithm to sustain a predefined number of localizations per frame. Typical acquisition parameters can be found in Supplementary Table 4. Coverslips containing prepared samples were placed into a custom build sample holder and 500 µl of suitable buffer, depending on the used cell line and experiment (Table 2), was added. To avoid a pH drift caused by accumulation of glucuronic acid in GLOX-buffers, the buffer solution was exchanged after about 2 h of imaging. Samples were imaged until close to all fluorophores were bleached and no further localizations were detected under continuous ultraviolet irradiation.

Pixel size calibration. The effective pixel size of the microscope was calibrated by translating fluorescent beads, immobilized on a coverslip, with a calibrated sample stage (SmarAct) that operated in close loop. From the measured translation of many beads the pixel size could be calibrated with a high accuracy.

Widefield, SIM and SRRF on expanded samples. After expansion (protocol described above) U2OS-Nup96-mEGFP cells labeled with an Atto488-coupled anti-GFP nanobody were imaged in a Zeiss Elyra PS.1 system. A ×100 TIRF objective (Plan-APOCHROMAT ×100/1.46 NA Oil, Zeiss) was used, with additional 1.6 magnification, to collect fluorescence onto an EMCCD camera (iXon Ultra 897, Andor), yielding a pixel size of 100 nm. The sample was illuminated with a 488 nm laser set at 150 mW cm⁻². Widefield images were collected with 100 ms exposure, SIM images with 100 ms exposure and five grid rotations, each SRRF image was generated from a frame burst of 100 images acquired at 33 Hz. SIM reconstructions were generated with the Zeiss Elyra Zen software using automatic settings. SRRF images were analyzed with NanoJ-SRRF[24] using standard settings. Images were validated for quality using SIMCheck[6] (structured illumination microscopy, SIM) and NanoJ-SQUIRREL[7] (SIM and SRRF).

Confocal microscopy. Fixed U2OS-Nup96-mEGFP samples on 35 mm glass bottom dishes were prepared according to the preparation protocol described above and imaged using an Olympus FV3000 laser scanning microscope. A ×60/1.40 NA oil immersion objective (Olympus, PLAPON 60XOSC2) was used in combination with a motorized stage, operated by the Fluoview software (Olympus). Pixel size was set to ~70 nm in x and y. Fluorescence emission went through a 550/100 bandpass filter and a 1.0 Airy unit (202 µm) wide pinhole before detection on four GaAsP spectral detectors. For each nucleus, a z stack, consisting of 3–5 planes 250 nm apart from each other, was acquired around the basal plane of the nucleus to obtain maximum fluorescence intensity for all NPCs.

Airy-scan microscopy. U2OS-Nup96-mEGFP cells grown in 35-mm glass-bottom dishes were fixed in accordance to the previously described protocol. A Zeiss LSM 880 with an additional Airy FAST detector module (Zeiss) was used for Airy-image acquisition in combination with a 63×/1.4 NA oil immersion objective (Zeiss, Plan-Apochromat 63×/1.4 NA Oil DIC M27). The system was operated by the ZEN software (Zeiss, black edition). Pixel size was set to ~40 nm in the x and y directions. Samples were focused on the basal plane of the nucleus and mEGFP was excited using a 488 nm laser. Emission was collected through a 495–550 nm bandpass filter, 570 nm longpass filter and a 1.25 Airy unit (~60 µm) pinhole onto the 32 GaAsP detector elements. A z stack, consisting of 3–5 slices 200 nm apart from each other around the basal plane was acquired for each nucleus. Post-processing was done with ZENs Airy-scan processing using automatic deconvolution parameters.

STED microscopy. Samples were prepared according to the protocol for nanobody staining of U2OS-Nup96-GFP samples and were imaged on an Abberior STED/RESOLFT microscope (Abberior Instruments, Expert Line) running the Inspector software (Abberior Instruments). The microscope comprises an IX83 stage (Olympus) in combination with a UPlan-S Apochromat ×100/1.40 NA oil objective

(Olympus). Pixel size was set to 15 nm in the x and y directions. Super-resolved images were acquired by donut-shaped depletion using a 775 nm pulsed laser along with a 640 nm pulsed laser, exciting STAR 635P tagged Nup96-mEGFP. A single plane of the lower side of the nucleus was imaged. Emission was collected through a 685/70 nm bandpass filter. We used a depletion power of approximately 150 mW in the sample. Higher depletion powers could, in principle, increase the resolution further, but in our case lead to strong bleaching and high noise for these rather dim samples.

Ratiometric dual-color SMLM. For ratiometric dual-color imaging of AF647 and CF680, the emitted fluorescence was split by a 665LP beamsplitter (catalog no. ET665lp, Chroma), filtered by a 685/70 (catalog no. ET685/70m, Chroma) bandpass filter (transmitted light) or a 676/37 (catalog no. FF01-676/37-25, Semrock) bandpass filter (reflected light) and imaged side by side on the EMCCD camera. The color of the individual blinks was assigned by calculating the ratio of the intensities in the two channels.

Astigmatic 3D SMLM. The 3D SMLM data was acquired using a cylindrical lens ($f = 1,000$ mm; catalog no. LJ1516L1-A, Thorlabs) to introduce astigmatism. The data were fitted and analyzed as described previously[61]. First, z stacks with known displacement of several (15–20) fields of view of TetraSpeck beads on a coverslip were acquired to generate a model of the experimental point spread function. This model was then used to determine the z position of the individual localizations. To correct for depth-dependent aberrations, we acquired stacks of beads in agarose to determine the fitting errors as described previously[30].

Data analysis. All data analysis was conducted with custom software written in MATLAB and is available as open source (github.com/jries/SMAP). Installation instructions are found in the README.md, and step-by-step guides on how to use the software to perform all analyses used in this manuscript are available via the Help menu.

Fitting. Two-dimensional data were fitted with a symmetric Gaussian PSF model (free fitting parameters: x, y, PSF size, photons per localization, background per pixel) using maximum likelihood estimation (MLE)[62]. Astigmatic 3D data were fitted with an experimentally derived PSF model (free fitting parameters: x, y, z, photons per localization, background per pixel), also using an MLE fitter[61].

Post-processing. The x, y and, when applicable, z positions were corrected for residual drift by a custom algorithm based on redundant cross-correlation. Localizations persistent over consecutive frames (detected within 35 nm from one another and with a maximum gap of one dark frame) were merged into one localization by calculating the weighted average of x, y and z positions and the sums of photons per localization and background. Localizations were filtered by the localization precision (0–10 nm for dSTORM, 0–25 nm for PALM) to exclude dim localizations, and for two-dimensional data by the fitted size of the PSF (0–150 nm laterally) to exclude localizations that were strongly out-of-focus. Additionally, poorly fitted localizations were excluded if their log-likelihood (LL) was smaller than the mean (LL)—3 × STD (LL). Superresolution images were constructed with every localization rendered as a two-dimensional elliptical Gaussian with a width proportional to the localization precision (factor 0.4). The reported mean photons per localization were calculated based on these merged and filtered localizations.

Determination of the expansion factor. To determine the local expansion factor from the Ex-SIM data set, we manually selected positions of 203 nuclear pores and fitted a cropped image of the pore with a model that consisted of a ring convolved with a Gaussian function, treating the radius and the standard deviation of the Gaussian as free fitting parameters. We then re-fitted the data keeping the standard deviation of the Gaussian fixed to its mean value. By comparing the mean value of the radius with that one measured on a calibrated SMLM microscope, we directly determined the expansion factor.

Segmentation. To automatically segment NPCs, we convolved the reconstructed superresolution image with a kernel consisting of a ring with a radius corresponding to the radius of the NPC, convolved with a Gaussian. Local maxima over a user-defined threshold were treated as candidate NPCs. These candidates included many aberrant structures. We cleaned up the segmentation by a two-step filtering process. (1) We fitted the localizations corresponding to each candidate with a circle to reject structures with very small (typically <40 nm) or very large (>70 nm) radii. (2) We re-fitted the localizations with a circle of fixed radius to determine its center coordinates, and rejected structures where more than 25% of the localizations were within 40 nm of the center (structures that visually did not resemble NPCs) or more than 40% of the localizations were further away than 70 nm (structures that were usually composed of two adjacent NPCs and wrongly segmented).

We segmented many data sets manually and compared that segmentation with the automatic segmentation and found an excellent agreement with less than 1.2% difference in measured ELE values and less than 5% error in the mean number of localizations per NPC.

Geometric analysis. All geometric analysis was carried out on NPCs segmented as described above, based on the coordinates of the localizations.

Analysis of profiles. Profiles in the xy plane were constructed by (1) selecting a linear region of interest (ROI) in the direction the profile is calculated, (2) selecting only localizations in a rectangular ROI along the line profile and with a given width, (3) rotating the coordinates such that the x' axis is along the direction of the line profile, (4) calculating a histogram of the x' coordinates. This histogram was then fitted with a single or double-Gaussian function. For profiles along the z direction we (1) defined a ROI, (2) calculated the histogram of z coordinates for localizations within this ROI and (3) fitted the histogram with a single or double-Gaussian function.

We want to stress that care must be taken that profiles are constructed from a sufficient number of localizations, and are never measured in a superresolution image where localizations are rendered with a Gaussian kernel. Otherwise even single localizations can result in 'profiles' with arbitrary small width and two random localizations can be 'resolved' if their distance is larger than the arbitrary kernel size. This holds true for any profile analysis of SMLM data and is not restricted to NPCs.

Radius of the NPC. The radius of the circular NPC structures was determined by directly fitting the coordinates of the localizations with a circular model treating the x and y coordinates and the radius as free fitting parameters.

Distance between cytoplasmic and nucleoplasmic rings in two-dimensional data. Ring distances were measured on two-dimensional data sets where the focus was set to the mid-plane of the nucleus. (1) We manually segmented structures on vertical parts of the nuclear envelope. (2) We constructed profiles perpendicular to the nuclear envelope with a width of 200 nm by calculating the histogram of rotated localizations. (3) We fitted the profiles with a double-Gaussian function to determine the distance of the rings.

Distance of cytoplasmic and nucleoplasmic rings from 3D data. Segmented localizations were fitted in three dimensions with a template describing two parallel rings with a fixed radius (mean of the radius as measured before) and variable x, y and z positions, rotation angles and distance between the rings. As a validation, we used the fitted rotation angles to rotate the localizations so that all NPCs were aligned and fitted the z profile with a double Gaussian as described above for two-dimensonal data.

Azimuthal angle. We determined the azimuthal angle between the cytoplasmic and nucleoplasmic rings from 3D data. (1) We fitted the localizations with a circle to determine its x and y center coordinates. (2) We determined the axial position of the NPC by fitting the z profile with a double-Gaussian as described above. (3) We separated localizations belonging to the upper and lower ring. (4) We transformed the x and y coordinates to polar coordinates. (5) We constructed histograms of the polar angles. (6) We calculated the auto- and cross-correlation curves of these histograms taking into account the circular boundary conditions. (7) We calculated the average correlation curves for all NPCs. (8) We fitted the average cross-correlation curve with a cosine function of fixed frequency and varying phase. We fitted the offset and amplitude of the trigonometric function by third-degree polynomials. We excluded the central 24° from the fit as they contained strong contributions from the re-activation of fluorophores. (9) The azimuthal angle corresponded to the fitted phase of the trigonometric function.

Determination of effective labeling efficiencies. To count the number of visible corners in each NPC we used the following approach. (1) The segmented and filtered localizations were fitted by a circle of fixed radius corresponding to the mean radius as determined before and coordinates were converted to polar coordinates ϕ_i, r_i. (2) Localizations too close to the center of the ring ($r_i < 30$ nm) or too far away ($r_i > 70$ nm) were excluded as background localizations. (3) We determined the rotation of the structure by minimizing

$$\phi_{\rm rot} = \arg\min_{\phi_{\rm rot}}\big(\phi_{\rm rot} - \phi_i \bmod \pi/4\big)$$

(4) We counted the number of segments containing a localization from a histogram of ϕ_i with a bin width of $\pi/4$ and a start bin of $\phi_{\rm rot} - \pi/8$. (5) We constructed a histogram of the number of corners of all NPCs in the data set and fitted it using the probabilistic model as described below, using the ELE as a free fitting parameter. (6) To calculate the statistical error, we used bootstrapping with typically 20 re-sampled data sets.

Probabilistic model for ELE. The binomial probability density function

$$B(k|n,p) = \binom{n}{k} p^k (1-p)^{n-k}$$

describes the probability of observing k successes in n independent trials, where the probability of success in any given trial is p. Thus, the probability of a corner of the NPC (consisting of four labels) to be dark is $p_{\rm dark} = B(0|4, p_{\rm label})$ and

the probability to see a corner with at least one label is $p_{bright} = 1 - p_{dark}$. The probability of N out of eight corners being bright and visible is:

$$p(N|p_{label}) = B(N|8, p_{bright}) = B(N|8, 1 - B(0|4, p_{label}))$$

Determination of number of localizations per fluorophore. The number of localizations (blinking events) N_b that are detected per fluorophore can be directly calculated from the ELE, the number of localizations per NPC N_l and the number of Nup96 molecules per NPC $N_{Nup96} = 32$:

$$N_b = \frac{N_l}{N_{Nup96}ELE}$$

Simulations. To validate our analysis routines, we performed realistic simulations based on a two-state (bright and dark) fluorophore model with bleaching[8]. (1) We defined the 3D coordinates of the 32 Nup96 proteins in the NPC based on our calibration (Fig. 2). (2) We randomly displaced all coordinates by a random vector and rotated the coordinates in three dimensions by random angles. (3) With a probability p_{label}, a protein was labeled and created a localization. (4) A labeled protein had a probability p_{react} to be reactivated. (5) Whenever a fluorophore was activated, it appeared at random during a frame and lived for t_l frames, determined as a random variable from an exponential distribution. (6) When it was on, a fluorophore had a constant brightness. (7) The emitted photons in each frame were determined as a random Poisson variable with a mean corresponding to the average brightness during the frame. (8) For each frame, we calculated the CRLB in x, y and z from the number of photons and the background[63]. (9) This error was added to the true x, y and z positions of the fluorophores as normally distributed random values with a variance corresponding to the respective calculated CRLB.

The simulated localizations were processed with the same data analysis pipeline as the real data.

Counting of protein copy numbers. <u>Counting in diffraction-limited microscopy using Nup96-mEGFP as a reference.</u> We used a simple data analysis procedure to compare the brightness of reference and target structures in confocal images. (1) We subtracted the image offset and, if required, corrected the images for photobleaching. (2) We calculated the maximum intensity projection of three frames around the focal plane of the nuclear pore structures and convolved the image with a Gaussian ($\sigma = 0.5$ pixels). (3) We up-sampled the image by a factor of two using cubic spline interpolation. (4) We determined all local maxima and chose a threshold based on the histogram of intensity values of those maxima. (5) We fitted the histogram of maxima intensities above the threshold with a Gaussian function to determine a robust estimate of the mean of the intensity values I_t and I_r for reference and target cell lines. (6) With N_r copies of the reference protein in the complex, the copy number in the target complex is then $N_t = N_r \langle I_t \rangle / \langle I_r \rangle$.

<u>Counting in mammalian cells using Nup96-mMaple as a reference.</u> (1) We automatically segmented reference and target data as described above and only considered nuclear pores in the focus (mean value of the fitted size of the PSF smaller than 145 nm). (2) We counted the number of merged localizations (L_r, L_t) in a circular ROI of a diameter of 220 nm. (3) From the mean number of localizations per NPC $\langle L_t \rangle$ and $\langle L_r \rangle$ we can calculate the copy number of the target complex $N_t = N_r \langle L_t \rangle / \langle L_r \rangle$.

<u>Counting in yeast cells using Nup188 as a reference.</u> (1) We manually segmented NPCs in yeast cells and excluded structures that were out of focus, at the edge of the nucleus or too close to other structures. (2) Based on the intensity of Abp1-mEGFP in a diffraction-limited channel we assigned all NPCs in a cell to belong to the reference cell line (significant mEGFP signal) or to the target cell line (no mEGFP signal). (3) We determined the number of localizations in a circular ROI of a diameter of 150 nm. (4) As above, we determined the mean number of merged localizations and from those the copy number of the target complex.

Model to estimate steady-state maturation fraction. Here, we derive a very simple model to estimate the fraction of matured photoconvertible fluorescent protein (for example, mMaple) in the steady state neglecting degradation. P denotes the amount of not yet matured protein, M the amount of the matured protein and k_m is the maturation rate. We assume exponential growth (growth rate k_g) of the organism and thus of the proteins:

$$\frac{dP}{dt} = k_g(P + M) - k_mP, \quad \frac{dM}{dT} = k_mP$$

The solution is:

$$\frac{P}{P + M} = \frac{e^{-(k_m + k_g)t}k_m + k_g}{k_m + k_g} \xrightarrow[t \to \infty]{} \frac{k_g}{k_m + k_g}$$

Assuming a doubling time for yeast of 120 min and a maturation time for mMaple of 48 min we find that in the steady state on average 28% of the mMaple is not yet matured. For mammalian cells (generation time 1 d) the fraction is reduced to 3.2%.

Software availability. All software is available at github.com/jries/SMAP.

Reporting Summary. Further information on research design is available in the Nature Research Reporting Summary linked to this article.

Data availability
All processed data (lists of localizations) and for each condition at least one example file of raw data (camera frames of blinking fluorophores) are deposited on BioStudies (https://www.ebi.ac.uk/biostudies/BioImages/studies/S-BIAD8).

References
51. Pleiner, T. et al. Nanobodies: site-specific labeling for super-resolution imaging, rapid epitope-mapping and native protein complex isolation. *eLife* **4**, e11349 (2015).
52. Göttfert, F. et al. Strong signal increase in STED fluorescence microscopy by imaging regions of subdiffraction extent. *Proc. Natl Acad. Sci. USA* **114**, 2125–2130 (2017).
53. Heilemann, M., Margeat, E., Kasper, R., Sauer, M. & Tinnefeld, P. Carbocyanine dyes as efficient reversible single-molecule optical switch. *J. Am. Chem. Soc.* **127**, 3801–3806 (2005).
54. Bates, M., Blosser, T. & Zhuang, X. Short-range spectroscopic ruler based on a single-molecule optical switch. *Phys. Rev. Lett.* **94**, 108101 (2005).
55. Koch, B. et al. Generation and validation of homozygous fluorescent knock-in cells using CRISPR–Cas9 genome editing. *Nat. Protoc.* **13**, 1465–1487 (2018).
56. Sun, X. et al. Development of SNAP-Tag fluorogenic probes for wash-free fluorescence imaging. *Chem. Bio. Chem.* **12**, 2217–2226 (2011).
57. Tillberg, P. W. et al. Protein-retention expansion microscopy of cells and tissues labeled using standard fluorescent proteins and antibodies. *Nat. Biotechnol.* **34**, 987–992 (2016).
58. Mund, M., Kaplan, C. & Ries, J. Localization microscopy in yeast. *Meth. Cell Biol.* **123**, 253–271 (2014).
59. Khmelinskii, A., Meurer, M., Duishoev, N., Delhomme, N. & Knop, M. Seamless gene tagging by endonuclease-driven homologous recombination. *PLoS ONE* **6**, e23794 (2011).
60. Deschamps, J., Rowald, A. & Ries, J. Efficient homogeneous illumination and optical sectioning for quantitative single-molecule localization microscopy. *Opt. Express* **24**, 28080–28090 (2016).
61. Li, Y. et al. Real-time 3D single-molecule localization using experimental point spread functions. *Nat. Methods* **15**, 367–369 (2018).
62. Smith, C. S., Joseph, N., Rieger, B. & Lidke, K. A. Fast, single-molecule localization that achieves theoretically minimum uncertainty. *Nat. Methods* **7**, 373–375 (2010).
63. Mortensen, K. I., Churchman, L. S., Spudich, J. A. & Flyvbjerg, H. Optimized localization analysis for single-molecule tracking and super-resolution microscopy. *Nat. Methods* **7**, 377–381 (2010).

Corresponding author(s): Jonas Ries

Last updated by author(s): 30.07.2019

Reporting Summary

Nature Research wishes to improve the reproducibility of the work that we publish. This form provides structure for consistency and transparency in reporting. For further information on Nature Research policies, see Authors & Referees and the Editorial Policy Checklist.

Statistics

For all statistical analyses, confirm that the following items are present in the figure legend, table legend, main text, or Methods section.

n/a	Confirmed	
☐	☒	The exact sample size (*n*) for each experimental group/condition, given as a discrete number and unit of measurement
☐	☒	A statement on whether measurements were taken from distinct samples or whether the same sample was measured repeatedly
☒	☐	The statistical test(s) used AND whether they are one- or two-sided *Only common tests should be described solely by name; describe more complex techniques in the Methods section.*
☒	☐	A description of all covariates tested
☒	☐	A description of any assumptions or corrections, such as tests of normality and adjustment for multiple comparisons
☐	☒	A full description of the statistical parameters including central tendency (e.g. means) or other basic estimates (e.g. regression coefficient) AND variation (e.g. standard deviation) or associated estimates of uncertainty (e.g. confidence intervals)
☒	☐	For null hypothesis testing, the test statistic (e.g. *F*, *t*, *r*) with confidence intervals, effect sizes, degrees of freedom and *P* value noted *Give P values as exact values whenever suitable.*
☒	☐	For Bayesian analysis, information on the choice of priors and Markov chain Monte Carlo settings
☒	☐	For hierarchical and complex designs, identification of the appropriate level for tests and full reporting of outcomes
☐	☒	Estimates of effect sizes (e.g. Cohen's *d*, Pearson's *r*), indicating how they were calculated

Our web collection on statistics for biologists contains articles on many of the points above.

Software and code

Policy information about availability of computer code

Data collection	SMLM Data collection was performed on custom microscopes detailed in the manuscript, using a custom written µManager (1.4.22; Open Imaging) plugin. Fluoview 2.3.1.163 Olympus (Confocal microscope) ZenBlack 2.3 SP1 FP2 Zeiss (Airy scan) Imspector 0.13.11885 Abberior Instruments (STED)
Data analysis	Data was curated and analyzed on custom code written in MATLAB R2019a (SMAP) which is detailed in the manuscript. SMAP has been deposited onto git (github.com/jries/SMAP) together with an analysis manual. ImageJ (Fiji) 1.8.0_172 NanoJ-SRRF: 1.14Stable1 SIMcheck 1.0.0 NanoJ-SQUIRREL 1.2 ZEN Black Version 11.0.2.190

For manuscripts utilizing custom algorithms or software that are central to the research but not yet described in published literature, software must be made available to editors/reviewers. We strongly encourage code deposition in a community repository (e.g. GitHub). See the Nature Research guidelines for submitting code & software for further information.

Data

Policy information about [availability of data](#)

All manuscripts must include a [data availability statement](#). This statement should provide the following information, where applicable:
- Accession codes, unique identifiers, or web links for publicly available datasets
- A list of figures that have associated raw data
- A description of any restrictions on data availability

> Manuscript contains data availability statement. All processed data (list of localizations) and for each condition at least one raw data file will be accessible on BioStudies, accession S-BSST257.

Field-specific reporting

Please select the one below that is the best fit for your research. If you are not sure, read the appropriate sections before making your selection.

☒ Life sciences ☐ Behavioural & social sciences ☐ Ecological, evolutionary & environmental sciences

For a reference copy of the document with all sections, see [nature.com/documents/nr-reporting-summary-flat.pdf](#)

Life sciences study design

All studies must disclose on these points even when the disclosure is negative.

Sample size	We did not do any sample size calculation. A minimum of 300 individual NPCs were analysed for each condition, which resulted in a low statistical variation. From our simulations (Supplementary Fig 7E) we determined that the above mentioned sample size was sufficient. Additionally these NPCs were pooled from different cells on different coverslips, and for most conditions from multiple biologically independent measurements, i.e. different cell culture passage numbers and preparations.
Data exclusions	Only data from experiments that obviously failed (wrong microscope setup/out-of-focus/ one outlier which was 7 sigma SD away) were excluded. Exclusion criteria were predetermined.
Replication	All replications were successful.
Randomization	Samples were not randomized. Our experimental workflow did not allow/need randomization.
Blinding	Blinding was not done. Our experimental workflow did not allow/need blinding.

Reporting for specific materials, systems and methods

We require information from authors about some types of materials, experimental systems and methods used in many studies. Here, indicate whether each material, system or method listed is relevant to your study. If you are not sure if a list item applies to your research, read the appropriate section before selecting a response.

Materials & experimental systems

n/a	Involved in the study
☐	☒ Antibodies
☐	☒ Eukaryotic cell lines
☒	☐ Palaeontology
☒	☐ Animals and other organisms
☒	☐ Human research participants
☒	☐ Clinical data

Methods

n/a	Involved in the study
☒	☐ ChIP-seq
☒	☐ Flow cytometry
☒	☐ MRI-based neuroimaging

Antibodies

Antibodies used	Anti-GFP FluoTag-Q-AF647 mEGFP NanoTag Biotechnologies; #N0301, Clones 1H1, (1:50 dilution) Anti-GFP FluoTag-Q-CF680 mEGFP NanoTag Biotechnologies; #N0301, Clones 1H1, (1:50 dilution) Anti-GFP FluoTag-X4-AF647 mEGFP NanoTag Biotechnologies; #N0304, Clones 1H1, 1B2, (1:50 dilution) Anti-GFP FluoTag-X4-CF680 mEGFP NanoTag Biotechnologies; #N0304, Clones 1H1, 1B2, (1:50 dilution) Anti-GFP FluoTag-X4-STAR 635P mEGFP NanoTag Biotechnologies; #N0304, Clones 1H1, 1B2, (1:50 dilution) Anti-GFP-IgG (rabbit) mEGFP MBL International; #598, Polyclonal ,(1:250 dilution) Homemade anti-rabbit-AF647 (donkey) IgG, Polyclonal, (1:300 dilution) Homemade nanobody against mEGFP tagged with AF647, no clone number, (1:50 dilution) pAb anti-nup98 LotA1, Novus, NB100-93325, Polyclonal, (1:2000) Anti-NUP107 (rabbit), SAB2702098, Lot#GT40268-64, Polyclonal, (1:1000)

Validation	Anti-GFP FluoTag-Q-mEGFP NanoTag Biotechnologies; #N0301, Clones 1H1 - Wagner et al. (2019) Myosin VI Drives Clathrin-Mediated AMPA Receptor Endocytosis to Facilitate Cerebellar Long-Term Depression DOI:https://doi.org/10.1016/j.celrep.2019.06.005 Anti-GFP FluoTag-X4-mEGFP NanoTag Biotechnologies; #N0304, Clones 1H1, 1B2 -Hussain et al. (2018) Inhibition of oxidative stress in cholinergic projection neurons fully rescues aging-associated olfactory circuit degeneration in Drosophila. Elife. 2018 Jan 18;7 PMID: 29345616 DOI: 10.7554/eLife.32018 -Fulterer et al. (2018) Active Zone Scaffold Protein Ratios Tune Functional Diversity across Brain Synapses DOI:https://doi.org/10.1016/j.celrep.2018.03.126 -Ravikumar et al. (2018) Independent yet overlapping pathways ensure the robustness and responsiveness of trans-Golgi network functions in Arabidopsis DOI: 10.1242/dev.169201 -Durand et al. (2018) A machine learning approach for online automated optimization of super-resolution optical microscopy DOI: 10.1038/s41467-018-07668-y Anti-GFP-IgG (rabbit) mEGFP MBL International; #598 -Engedal N, et al., All-trans retinoic acid stimulates IL-2-mediated proliferation of human T lymphocytes: early induction of cyclin D3. J Immunol. 177:2851-61. (2006), Anti-rabbit-AF647 (donkey) - Our data presented in the paper validates the antibody. Homemade nanobody against mEGFP tagged with AF647 - Our data presented in the paper validates the nanobody. pAb anti-nup98 LotA1, Novus, NB100-93325, - validated in our paper. Anti-NUP107 (rabbit), SAB2702098, Lot#GT40268-64 - validated in our paper

Eukaryotic cell lines

Policy information about cell lines

Cell line source(s)	ATCC-HTB-96, Lot # 61074667 Flp-In ™ T-REx ™ 293 Cell Line - were a gift from Edward Lemke
Authentication	Cell lines were not further authenticated.
Mycoplasma contamination	Cell lines have been tested and are negative for mycoplasma contamination.
Commonly misidentified lines (See ICLAC register)	No commonly misidentified cell lines were used.